CHALMERS
UNIVERSITY OF TECHNOLOGY

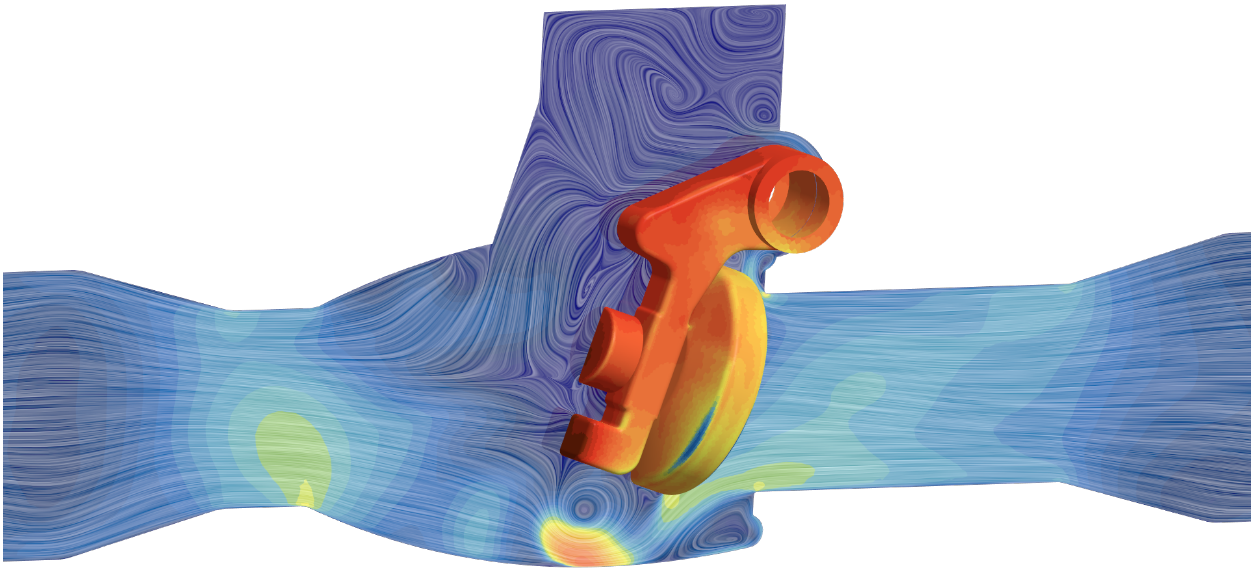

# CFD Study of a Clattering Swing Check Valve During Sudden Pressure Transients

## A Comparison Between RELAP5 and STAR-CCM+

Degree project report in Applied Mechanics

JAKOB OLSSON

DEPARTMENT OF MECHANICS AND MARITIME SCIENCES
CHALMERS UNIVERSITY OF TECHNOLOGY

Gothenburg, Sweden 2026
www.chalmers.se

Degree project report 2026

# CFD Study of a Clattering Swing Check Valve During Sudden Pressure Transients

A Comparison Between RELAP5 and STAR-CCM+

JAKOB OLSSON

Department of Mechanics and Maritime Sciences
Chalmers University of Technology
Gothenburg, Sweden 2026

CFD Study of a Clattering Swing Check Valve During Sudden Pressure Transients
A Comparison Between RELAP5 and STAR-CCM+
JAKOB OLSSON



Supervisor: Anna Jarenfors, FS Dynamics
Examiner: Niklas Andersson, Department of Mechanics and Maritime Sciences

Degree project report 2026
Department of Mechanics and Maritime Sciences
Chalmers University of Technology
SE-412 96 Gothenburg
Sweden
Telephone +46 31 772 1000

Cover: Pressure and velocity flow visualization around a swing check valve, showing streamlines colored by velocity magnitude through the pipe and a pressure contour on the valve surface.

Typeset in LaTeX
Gothenburg, Sweden 2026

CFD Study of a Clattering Swing Check Valve During Sudden Pressure Transients
A Comparison Between RELAP5 and STAR-CCM+
JAKOB OLSSON
Department of Mechanics and Maritime Sciences
Chalmers University of Technology

# Abstract

Swing check valves are used throughout piping networks to prevent sustained backflow following abnormal events such as a pipe break. System-level simulations have shown that pressure waves originating from such events can induce rapid clattering of check valves even far from the initiating disturbance, where the fluid is otherwise stationary. This thesis investigates the dynamic response of one such valve, comparing predictions from the 1D system code RELAP5 against compressible 3D computational fluid dynamics (CFD) simulations in STAR-CCM+.

The results show that RELAP5 predicts substantially faster and more aggressive valve motion than STAR-CCM+: while STAR-CCM+ reaches a single full opening before settling into a damped oscillation around a partial opening angle, RELAP5 repeatedly cycles between open and closed throughout the simulation. This discrepancy was traced to three contributing factors: an underestimation of the valve's effective inertia due to the absence of added mass and other hydrodynamic effects in the 1D model; an overestimated hydraulic force arising from RELAP5's pressure extrapolation and area assumptions; and a deviation between the loss coefficient predicted by RELAP5's angle-dependent scaling and that obtained from STAR-CCM+ at intermediate opening angles. As a result, RELAP5 likely overpredicts the severity of the associated water hammer effect, though the present results do not allow a definitive conclusion on the validity of the originally predicted clattering behavior.

As a secondary objective, torque coefficients required to implement an alternative RELAP5 check valve model were extracted from steady-state and transient 3D CFD simulations. The resulting model, however, was found to be poorly constrained outside the conditions explicitly simulated, and could not be meaningfully evaluated against the 3D results within the scope of this thesis.

Keywords: swing check valve, STAR-CCM+, RELAP5, fluid–structure interaction, valve clattering.

# Acknowledgements

I would like to thank my supervisor, Anna Jarenfors at FS Dynamics, for her guidance and feedback throughout this project. I am also grateful to my examiner, Niklas Andersson at the Department of Mechanics and Maritime Sciences, for introducing me to the fascinating subject of fluid mechanics. Thanks to the good people at FS Dynamics for an enjoyable working environment during the project. Finally, I want to thank my family and friends — those from before and the ones I made along the way — for their unconditional support throughout my studies. As the Beatles so aptly put it, *I get by with a little help from my friends.*

Jakob Olsson, Gothenburg, June 2026

# List of Acronyms

Below is the list of acronyms that have been used throughout this thesis listed in alphabetical order:

**BC** boundary condition 14, 16–22, 27, 35, 36, 42, III

**CFD** computational fluid dynamics v, 1, 2, 5, 12, 13, 16, 20, 24, 31, 35, 37, 43

**DFBI** dynamic fluid–body interaction 6, 7, 16, 19, 20, 25, 26, 32

**FDM** finite difference method 5

**FEM** finite element method 5

**FSI** fluid–structure interaction 6

**FVM** finite volume method 5

**IAPWS-IF97** International Association for the Properties of Water and Steam, Industrial Formulation 1997 18

**NIST** National Institute of Standards and Technology 29

**PDE** partial differential equation 3

**RANS** Reynolds-averaged Navier–Stokes 5

# Nomenclature

Below is the nomenclature of indices and variables that have been used throughout this thesis.

## Indices

| | |
|---|---|
| $f$ | Cell face index |
| $i, j, k$ | Spatial coordinate or tensor indices |

## Variables

| | |
|---|---|
| $\mathbf{A}_f$ | Cell face area vector |
| $A_p$ | Valve disc area |
| $c$ | Speed of sound |
| $C_\mu$ | Turbulence model constant |
| $C_{HS}$ | Static torque coefficient |
| $C_{HR}$ | Rotational torque coefficient |
| $D_{\text{outer}}$ | Disc outer diameter |
| $D_{\text{inner}}$ | Disc inner diameter |
| $e$ | Specific internal energy |
| $\mathbf{F}_b$ | Buoyancy force |
| $\mathbf{F}_g$ | Gravitational force |
| $\mathbf{F}_h$ | Hydraulic force |
| $F_i$ | Body force component |
| $\mathbf{g}$ | Gravitational acceleration |
| $\mathbf{I}$ | Moment of inertia tensor |
| $\mathbf{I}_{\text{AM}}$ | Added-mass moment of inertia |
| $\mathbf{I}_{\text{eff}}$ | Effective moment of inertia |
| $\mathbf{I}_{\text{mech}}$ | Mechanical moment of inertia |

| | |
|---|---|
| $k$ | Turbulent kinetic energy |
| $k_{1-6}$ | Regression Coefficients in the $\bar{C}_{HR}$ model |
| $K$ | Loss coefficient |
| $L$ | Total pipe length |
| $M$ | Mass of the rotating components |
| $m$ | Mass of displaced fluid |
| $p$ | Static pressure |
| $\Delta p$ | Pressure drop |
| $\mathbf{r}_{\text{COG}}$ | Position vector from the axis of rotation to the center of gravity |
| $\mathbf{r}_f$ | Position vector from the axis of rotation to the cell face center |
| $R$ | Distance between the axis of rotation and the center of gravity |
| $T$ | Temperature |
| $u_i$ | Velocity component |
| $\bar{u}_i$ | Mean velocity component |
| $u_i'$ | Fluctuating velocity component |
| $V$ | Characteristic flow velocity |
| $V_{in}$ | Inlet velocity; used specifically in the context of the $\bar{C}_{HR}$ regression model (Eq. 2.22) |
| $\dot{V}_{in}$ | Rate of change of inlet velocity |
| $\mathcal{V}$ | Volume of the rigid body |
| $v_{\text{rel}}$ | Relative fluid velocity |

| | |
|---|---|
| $\delta_{ij}$ | Kronecker delta |
| $\varepsilon$ | Dissipation rate of turbulent kinetic energy |
| $\lambda$ | Bulk viscosity coefficient |
| $\mu$ | Dynamic viscosity |
| $\nu_t$ | Eddy viscosity |
| $\omega$ | Specific rate of dissipation of turbulent kinetic energy |
| $\dot{\boldsymbol{\theta}}$ | Angular velocity |
| $\rho_f$ | Fluid density |
| $\rho_b$ | Density of the rigid body |
| $\tau_{ij}$ | Viscous stress tensor |
| $\bar{\tau}_{ij}$ | Mean viscous stress tensor |
| $\boldsymbol{\tau}$ | Torque |

| | |
|---|---|
| $\boldsymbol{\tau}_g$ | Gravitational torque |
| $\boldsymbol{\tau}_h$ | Hydraulic torque |
| $\theta$ | Valve opening angle |
| $\dot{\theta}_{\mathrm{pre}}$ | Prescribed check valve angular velocity |
| $\varphi$ | Pipe inclination angle |

# Contents

# List of Figures

# List of Tables

# 1 Introduction

## 1.1 Background

In nearly all major industrial mechanical systems, a piping network is responsible for transporting fluid from one place to another in a deliberate and carefully designed way. Most often, that is at a steady pace where pressures and velocities vary slowly with time. However, during abnormal events, such as a pipe break, the flow field can change drastically within milliseconds. The sudden depressurization will cause rapid flow reversal in sections of the piping network, which can have disastrous effects on the integrity and performance of the system.

Check valves are components designed to prevent sustained backflow. They come in a wide variety of designs, but the swing check valve is among the most commonly used. Mounted inside the pipe, it opens when fluid flows through it in the intended direction and remains open as long as the momentum of the fluid exceeds the weight of the valve itself. Should an accident cause the flow to suddenly reverse, the check valve closes rapidly and limits the extent of the potential damage.

Check valve closure is not, however, without consequences. If the fluid still carries momentum when the valve is fully closed, it impacts the valve disc with a substantial force, generating pressure waves that propagate throughout the piping network — a phenomenon commonly referred to as water hammer — with pressure spikes that may exceed the design limits of the system.

In a large piping network, check valves are positioned at multiple locations throughout the system to ensure correct operation. The focus of this thesis is on check valves located far from the accident site, specifically in auxiliary feedwater pipes that are on standby, where the water is initially stationary. In such conditions, a swing check valve rests fully closed against its seat. However, system-level simulations made by FS Dynamics for a customer operating in the nuclear energy sector have shown that pressure waves propagating from the accident site can induce rapid clattering of these check valves, although they are situated far from the initiating event.

In the nuclear industry, one-dimensional (1D) models are commonly used to simulate piping systems. RELAP5 is a software developed specifically for transient analysis of light water reactors [1]. While computationally efficient, 1D models have a limited ability to capture the complex flow features associated with sudden pressure transients. Three-dimensional (3D) computational fluid dynamics (CFD) simulations offer the possibility to investigate these effects in greater detail. Determining how the predictions from 3D CFD compare with those of RELAP5 for industrial applications is therefore of practical importance.

Previous master's theses investigating the dynamics of swing check valves have primarily focused on valves located in the immediate vicinity of the initiating disturbance. In contrast, the present thesis considers an initially closed valve situated in an adjacent piping system that, ideally, should remain unaffected by the disturbance, yet has been observed to exhibit motion. Whereas earlier studies assumed incompressible flow, the present thesis accounts for fluid compressibility to accurately capture the dynamics of the check valve during a sudden pressure transient.

## 1.2 Purpose

The purpose of this master's thesis is to investigate the dynamic response of a swing check valve located far from the initiating disturbance during a sudden pressure transient. The primary objective is to recreate an event in which the RELAP5 model has predicted clattering, and to simulate the same event using compressible 3D CFD in STAR-CCM+. By comparing the results of both models, the study aims to evaluate the predictive capability of the 1D model, assess the validity of the predicted clattering behavior, and investigate the root cause of any discrepancies between the models.

A secondary objective is to determine torque coefficients for an alternative swing check valve formulation in RELAP5, using steady-state and transient CFD simulations. These parameters enable the alternative model to be implemented and evaluated against the STAR-CCM+ simulations.

## 1.3 Limitations

The thesis is limited to a simplified section of an auxiliary feedwater pipe within a piping network and does not include a full system-level representation. The analysis is restricted to a single check valve located far from the initiating disturbance. Structural deformation is neglected; the valve and pipe components are treated as rigid bodies. To limit computational cost, transient behavior on time scales much longer than the pressure disturbance is not simulated.

# 2

# Theory

Governing Equations — STAR-CCM+ — RELAP5

This chapter is divided into three main sections. The first covers the governing equations of fluid mechanics and other relevant fundamental principles. This is followed by a description of the numerical methods used in STAR-CCM+ and the theory of DFBI. Finally, the RELAP5 check valve model formulations used in this thesis are presented.

## 2.1 Governing Equations of Fluid Mechanics

### 2.1.1 The Navier–Stokes Equations

The Navier–Stokes equations are a set of partial differential equations (PDEs) that describe the motion of Newtonian fluids [2]. Only a brief overview of their physical interpretation is provided here. The following is based on Anderson [3].

The equations consist of three fundamental conservation laws: conservation of mass, momentum, and energy. Due to their complexity, it is often necessary to make simplifying assumptions about which phenomena are relevant for the flow under investigation. For instance, liquid water at moderate pressures is generally treated as incompressible, allowing several terms to be eliminated. However, for the case studied in this thesis — where pressure waves play a significant role — the compressible form of the equations is required. The equations are here expressed using the control volume formulation, representing an arbitrary finite region of the flow,

**Conservation of mass**

$$\frac{\partial \rho_f}{\partial t} + \frac{\partial(\rho_f u_j)}{\partial x_j} = 0 \tag{2.1}$$

**Conservation of momentum**

$$\rho_f \left( \frac{\partial u_i}{\partial t} + u_j \frac{\partial u_i}{\partial x_j} \right) = -\frac{\partial p}{\partial x_i} + \frac{\partial \tau_{ij}}{\partial x_j} + f_i \tag{2.2}$$

$$\text{where } \tau_{ij} = \mu \left( \frac{\partial u_i}{\partial x_j} + \frac{\partial u_j}{\partial x_i} \right) + \left( \lambda - \frac{2}{3}\mu \right) \frac{\partial u_k}{\partial x_k} \delta_{ij},$$

and $\lambda$ is the bulk viscosity coefficient.

**Conservation of energy**

$$\rho_f \frac{De}{Dt} = -p\frac{\partial u_k}{\partial x_k} + \tau_{ij}\frac{\partial u_i}{\partial x_j} + \frac{\partial}{\partial x_j}\left( k \frac{\partial T}{\partial x_j} \right) \tag{2.3}$$

The conservation of mass, more commonly referred to as the continuity equation, states that mass is conserved within a control volume. This is satisfied either by the fluid entering the control volume at the same rate as it exits (the second term), by a change in the local fluid density within the control volume (the first term), or by a combination of both.

The conservation of momentum consists of three equations, one for each component of the velocity vector, and is analogous to Newton's 2nd law, $\frac{\partial}{\partial t}(m\mathbf{u}) = \sum \mathbf{F}$. In this analogy, the left-hand side of Eq. (2.2) represents the rate of change of momentum, and the right-hand side represents the sum of forces acting on the control volume. The first term on the right-hand side is a driving force produced by the pressure gradient across the control volume, the second term $(\nabla \cdot \boldsymbol{\tau})$ represents frictional forces due to the viscosity of the fluid, and $\mathbf{f}$ represents any external body forces such as gravity or electromagnetic forces.

The conservation of energy equation is analogous to the first law of thermodynamics, stating that energy within a control volume cannot be created or destroyed — only transferred between the control volume and its surroundings, or converted from one form to another, such as kinetic energy being converted to heat.

The unknown variables in these equations are the three components of the velocity vector $(u_x, u_y, u_z)$, the pressure $(p)$, the fluid density $(\rho_f)$ and the specific internal energy $(e)$. This gives six unknowns but only five equations. To close the system, a sixth equation is required, provided by the thermodynamic equation of state of the fluid.

### 2.1.2 Turbulence modeling

Modeling turbulence is one of the greatest challenges in fluid mechanics. The most common approach is to decompose the velocity and pressure fields into a mean and a fluctuating part, $u_i = \bar{u}_i + u_i'$ and $p = \bar{p} + p'$. Substituting this decomposition into the momentum equation (Eq. 2.2) and applying time-averaging yields the Reynolds-averaged Navier–Stokes (RANS) momentum equation [4],

$$\rho_f \left( \frac{\partial \bar{u}_i}{\partial t} + \bar{u}_j \frac{\partial \bar{u}_i}{\partial x_j} \right) = -\frac{\partial \bar{p}}{\partial x_i} + \frac{\partial}{\partial x_j} \left( \bar{\tau}_{ij} - \rho_f \overline{u_i' u_j'} \right) + f_i. \tag{2.4}$$

From this reformulation, an additional unknown term $\rho_f \overline{u_i' u_j'}$, commonly known as the Reynolds stress tensor, appears. Since there is now one more unknown than there are equations, an additional equation must be included to close the system.

The Boussinesq hypothesis states that the Reynolds stress tensor can be approximated from the mean flow properties as [4],

$$-\overline{u_i' u_j'} = \nu_t \left( \frac{\partial \bar{u}_i}{\partial x_j} + \frac{\partial \bar{u}_j}{\partial x_i} \right) - \frac{2}{3} k \delta_{ij}, \tag{2.5}$$

where $k = \frac{1}{2}\overline{u_i' u_i'}$ is the turbulent kinetic energy and $\nu_t$, the eddy viscosity, is a proportionality constant.

The eddy viscosity can be modeled in a number of ways, but two of the most common models in industrial CFD are the $k-\varepsilon$ and $k-\omega$ models [4]. Their names come from the quantities used to determine $\nu_t$: $\varepsilon$, the rate of dissipation of turbulent kinetic energy, and $\omega$, the specific rate of dissipation of turbulent kinetic energy,

$$\nu_{t,k-\varepsilon} = C_\mu \frac{k^2}{\varepsilon}, \quad \nu_{t,k-\omega} = \frac{k}{\omega}, \tag{2.6}$$

where $C_\mu$ is a modeling constant.

Generally, $k-\omega$ is considered to perform better near walls, whereas $k-\varepsilon$ performs better in free-stream and wake regions. The $k-\omega$ SST model was developed to combine the strengths of both, transitioning between the two based on the distance to the nearest wall [5].

## 2.2 STAR-CCM+

### 2.2.1 The Finite Volume Method

STAR-CCM+ is a CFD software that uses the finite volume method (FVM) to discretize and solve the Navier–Stokes equations. The basic idea behind the method is that a large fluid domain is divided into a finite number of smaller control volumes, referred to as cells, where the conservation laws must be satisfied both locally and globally across the entire domain. The collection of cells forms the computational mesh, where neighboring cells are connected through shared faces [6].

Mesh cells must be small enough that fluid properties, such as pressure, velocity, and temperature, can be represented as constant, cell-averaged values. The FVM differs from other numerical approaches, such as the finite difference method (FDM) and finite element method (FEM), in that the governing equations are integrated across each cell [7]. The resulting discretized quantities are then typically stored at the cell centers, which is the approach used in STAR-CCM+ [8].

### 2.2.2 Segregated and Coupled Solvers

To solve the discretized governing equations, a numerical solution algorithm must be used. In STAR-CCM+, two main solution strategies are available: the segregated and coupled solvers.

Velocity and pressure are coupled in the continuity and momentum equations (Eqs. (2.1) and (2.2)), meaning they cannot be solved independently of one another. In a segregated solver, the governing equations are solved sequentially. Typically, this means that an initial pressure field is assumed, allowing the velocity field to be obtained from the momentum equations. Using this velocity field, a pressure-correction equation derived from the continuity equation is solved to update the pressure field and enforce local conservation of mass. These steps are then repeated iteratively until convergence is achieved and the continuity equation is satisfied throughout the entire domain. If the pressure–velocity coupling is strong, many iterations may be required for the pressure and velocity fields to converge. This approach forms the basis of pressure–velocity coupling algorithms such as SIMPLE and PISO [6, 8].

In contrast, coupled solvers solve the governing equations for velocity, pressure, and temperature in all cells simultaneously as part of one large system of equations. Density is then obtained from the thermodynamic equation of state after the thermodynamic properties have been computed [9, 8]. Coupled solvers typically require higher memory usage but have been known to reduce computational time and improve convergence for strongly coupled flows, such as compressible flows [10].

### 2.2.3 Dynamic Fluid Body Interaction

Dynamic fluid–body interaction (DFBI) is a specific type of fluid–structure interaction (FSI), used to model the motion of a rigid body in response to the forces and moments acting on it from the surrounding fluid. Under the rigid body assumption, it is sufficient to solve the equations of motion for the body's center of mass [8].

#### 2.2.3.1 Single-Degree-of-Freedom Rotational Motion

From Newton's 2nd law of rotation, the dynamics of a body rotating around a fixed hinge axis can be described as

$$\mathbf{I}\frac{\partial \dot{\boldsymbol{\theta}}}{\partial t} = \sum \boldsymbol{\tau}, \tag{2.7}$$

where $\dot{\boldsymbol{\theta}}$ is the angular velocity of the body, $\mathbf{I}$ the moment of inertia and $\boldsymbol{\tau}$ the torque applied to the body [11]. In 3D, both $\mathbf{I}$ and $\boldsymbol{\tau}$ are tensors, but with the restriction of motion to a single degree of freedom, only the components acting within that degree of freedom are of interest. For instance, if the body rotates around a hinge axis parallel to the $y$–axis of the local coordinate system, only the $\tau_{yy}$ and $I_{yy}$ components contribute to the motion.

The moment of inertia tensor describes how the mass of a body is distributed relative to a given axis, and thus how it resists rotational acceleration about that axis. The tensor is defined as

$$I_{ij} = \int \rho_b (x_k x_k \delta_{ij} - x_i x_j) dV, \tag{2.8}$$

where $\delta_{ij}$ is the Kronecker delta and equals 1 when $i = j$, and 0 otherwise [11].

The moment of inertia of a body can be decomposed into two contributions: (1) the mechanical moment of inertia, arising from the geometric shape and mass distribution of the body, and (2) an additional inertia due to the added mass effect [12]. Whether the latter effect is significant depends primarily on the shape of the body and the medium in which it moves. In essence, added mass arises from the fact that an accelerating body must not only overcome its own inertia, but also accelerate the fluid displaced by its motion and the fluid near its surface due to the no-slip condition. The effective moment of inertia can therefore be written as

$$\mathbf{I}_{\text{eff}} = \mathbf{I}_{\text{mech}} + \mathbf{I}_{\text{AM}}. \tag{2.9}$$

For a cylinder in water, the added mass can be as large as the displaced mass of fluid [12]. For rigid bodies with simple geometry, $\mathbf{I}_{\text{mech}}$ can be derived analytically using standard formulas and shifted to the desired axis via the parallel-axis theorem [11]. For more complex geometries, it can instead be obtained directly from CAD-capable software such as STAR-CCM+ or ANSYS SpaceClaim.

The torque acting on the body arises mainly from two sources: the gravitational force ($F_g$), and the hydraulic force exerted by the surrounding fluid ($F_h$). The gravitational torque can be written as,

$$\boldsymbol{\tau}_g = \mathbf{r}_{\text{COG}} \times \mathbf{F}_g = \mathbf{r}_{\text{COG}} \times \rho_b \mathcal{V} \mathbf{g}, \tag{2.10}$$

where $\mathbf{r}_{COG}$ is the position vector from the axis of rotation to the body's center of gravity, $\rho_b$ its density, and $\mathcal{V}$ its volume. To obtain the hydraulic torque, the pressure and shear stress are integrated across the body surface. For a discrete body, the integral becomes a summation across all surface cell faces,

$$\boldsymbol{\tau}_h = \sum \mathbf{r}_f \times \mathbf{F}_h = \sum \left( \mathbf{r}_f \times p_f \mathbf{A}_f \right) - \sum \left( \mathbf{r}_f \times \boldsymbol{\tau}_f \mathbf{A}_f \right), \tag{2.11}$$

where $p_f$ and $\boldsymbol{\tau}_f$ are the pressure and shear stress acting on each cell face, and $\mathbf{r}_f$ is the position vector from the axis of rotation to the cell face center. The hydrostatic torque due to buoyancy is implicitly included in this formulation.

In summary, the equation of rotational motion can be written as

$$\left( \mathbf{I}_{\text{mech}} + \mathbf{I}_{\text{AM}} \right) \frac{\partial \dot{\boldsymbol{\theta}}}{\partial t} = \boldsymbol{\tau}_g + \boldsymbol{\tau}_h. \tag{2.12}$$

This equation governs the rotational motion of the swing check valve and forms the basis of the DFBI implementation in STAR-CCM+ [8].

## 2.3 RELAP5

Two swing check valve models are used in this thesis, neither of which is the original, built-in RELAP5 check valve type. The force-based model is implemented using the `SRVVLV` (servo valve) component, where the force balance governing the valve dynamics is defined through control variables. The alternative `th_sr` model is instead implemented using the `SWCVLV` (swing check valve) component, which is a more recent addition to the RELAP5 component library [1].

### 2.3.1 Force-Based Swing Check Valve Model

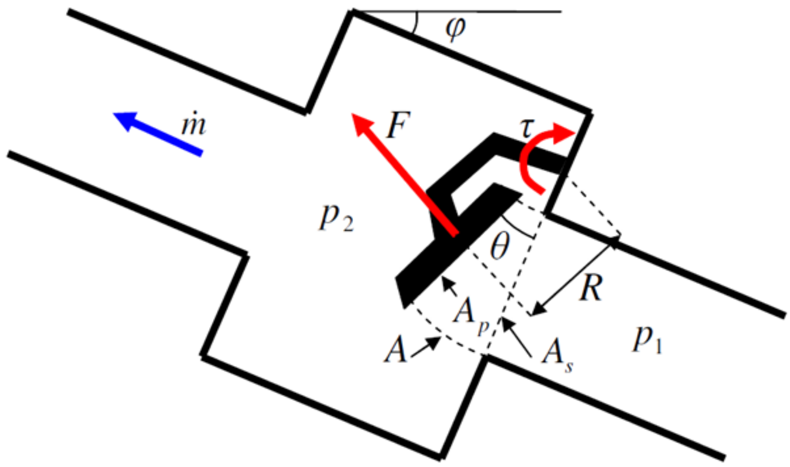


**Figure 2.1:** Schematic drawing of a swing check valve. Reproduced from [13].

The following is based on [13]. A schematic drawing of the force-based model is shown in Fig. 2.1. Unlike the STAR-CCM+ formulation, the RELAP5 model assumes that all forces generating torque act at the center of gravity, and the buoyancy force is treated explicitly rather than implicitly. The hydraulic force is decomposed into a fluid momentum force ($F_h$) and a buoyancy force ($F_b$), so the equation of motion in RELAP5 takes the form[1]

$$I\frac{d\dot{\theta}}{dt} = \sum \tau = (F_g + F_b + F_h)\, R, \tag{2.13}$$

where $R$ denotes the distance between the axis of rotation and the center of gravity, corresponding to $|\mathbf{r}_{COG}|$ in the previous notation.

If the pipe segment containing the check valve is horizontally oriented, the inclination angle $\varphi = 0$ in Fig. 2.1, and the gravitational and buoyancy forces acting on the check valve become,

$$F_g = -Mg\cos(\theta) \quad \text{and} \quad F_b = mg\cos(\theta), \tag{2.14}$$

[1]In the RELAP5 notation, $F_h$ denotes only the fluid momentum contribution, whereas in Eq. 2.11 it includes additional implicit hydrodynamic contributions such as buoyancy.

where $M$ and $m$ are the mass of the rotating parts and the displaced fluid, respectively, and $\theta$ is the valve opening angle.

The fluid momentum force, $F_h$, is implemented as a discretized 1D approximation of the momentum equation (Eq. 2.2), assuming steady, inviscid flow without body forces,

$$F_h = A_p \left(\Delta p - \rho_f |v_{rel}| v_{rel}\right) \tag{2.15}$$

where $A_p$ is the area of the valve disc, $\Delta p = p_1 - p_2$ is the difference in static pressure on the upstream and downstream surfaces of the valve, and $\rho_f |v_{rel}| v_{rel}$ is the dynamic pressure arising from the fluid velocity relative to the moving valve disc. Since static pressure is evaluated at the centers of the adjacent pipe elements in RELAP5, it must be extrapolated to the valve surfaces. As the cross-sectional area may vary between elements — causing significant changes in velocity — total pressure is used for the extrapolation rather than static pressure.

The resulting force acting on the check valve surfaces can thereby be written as

$$F = F_h + F_b + F_g \tag{2.16}$$

### 2.3.2 `th_sr` Swing Check Valve Model

The `th_sr` model, based on the theory by Li and Liou [14], determines disc motion from the hydraulic torque acting on the valve, rather than from the pressure-force formulation of Sec. 2.3.1. Only a brief theoretical overview is given here; for a full description, the reader is referred to [14].

The total hydraulic torque acting on the disc, $\tau_H$, can be divided into a stationary and a rotational contribution,

$$\tau_H = \tau_{HS} + \tau_{HR}, \tag{2.17}$$

where the static and rotational components are computed as [14],

$$|\tau_{HS}| = C_{HS} \rho_f A_p \frac{V^2}{2} R, \tag{2.18}$$

$$|\tau_{HR}| = C_{HR} \rho_f A_p \frac{(R\dot{\theta})^2}{2} R \tag{2.19}$$

When the disc is stationary, the only contribution to the total torque is the static torque, $\tau_{HS} = \tau_H$. In transient simulations, however, the static and rotational contributions in Eq. 2.17 cannot be separated directly. The rotational torque is therefore obtained by subtracting the static contribution from the total torque, $\tau_{HR} = \tau_H - \tau_{HS}$ [15].

Substituting this expression into Eq. 2.19, the static and rotational torque coefficients can be expressed as

$$C_{HS} = \frac{2|\tau_{HS}|}{\rho_f A_p V^2 R} \tag{2.20}$$

$$C_{HR} = \frac{2|\tau_H - \tau_{HS}|}{\rho_f A_p R (R\dot{\theta})^2} \tag{2.21}$$

In the implementation of the `th_sr` model in RELAP5, $C_{HR}$ is represented by the quadratic regression model

$$C_{HR} \approx \bar{C}_{HR} = k_1 + k_2\dot{\theta} + k_3 V + k_4\dot{\theta}V + k_5\dot{\theta}^2 + k_6 V^2, \tag{2.22}$$

where $V$ is the inlet velocity and $\dot{\theta}$ the angular velocity of the check valve.

### 2.3.3 Loss Coefficient

Whenever a check valve is installed in a pipe system, it introduces an energy loss to the flow. The loss coefficient quantifies the magnitude of this loss for a given valve and is defined as

$$K = \frac{\Delta p}{\frac{1}{2}\rho_f V^2} = \frac{2\rho_f A^2 \Delta p}{\dot{m}^2} \tag{2.23}$$

It can be obtained experimentally by measuring the pressure drop across two locations on either side of the valve while fluid passes through at a known, constant flow rate. The measurement locations must be sufficiently far from the valve that the flow has fully recovered. The loss coefficient is typically provided by the manufacturer and can vary significantly depending on the valve design [2]. In RELAP5, the loss coefficient is specified as an input parameter when defining the swing check valve model, but only as a scalar value corresponding to the check valve in its fully open position. For intermediate valve angles, RELAP5 scales the fully open loss coefficient using an empirical correlation based on the Borda–Carnot model [16].

# 3
# Methodology

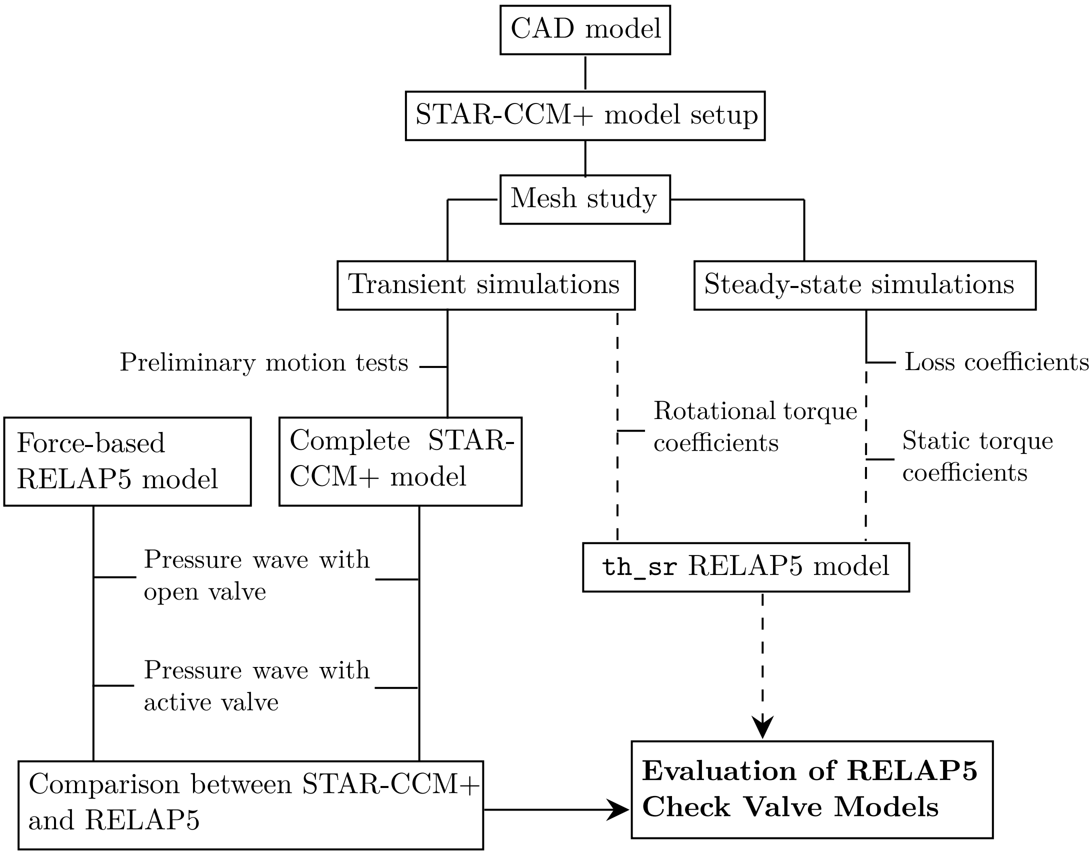


**Figure 3.1:** The thesis workflow chart.

This section describes the methodology adopted to achieve the objectives of the thesis. An overview of the methodology is shown in the thesis workflow chart, Fig. 3.1. Although the chart may initially appear complex, each component is explained in detail throughout this section.

The methodology related to the primary objective is presented first and follows the solid-line path. This involves evaluating the force-based RELAP5 model against the corresponding 3D simulations performed in STAR-CCM+. The secondary objective, represented by the dashed line, is presented thereafter, and concerns the implementation and evaluation of the `th_sr` model.

## 3.1 CAD Model

The domain geometry is based on a simplified section of an auxiliary feedwater piping system, with certain T-sections removed, modeled in ANSYS SpaceClaim from technical drawings. The pipe contains a single swing check valve. Prior to importing the geometry into the CFD software, two modifications were made: the check valve was rotated to its fully open position of 56°, and the geometry was partitioned into three distinct bodies — one enclosing the check valve and two representing the pipe sections on either side of the valve.

The complete pipe geometry is shown in Fig. 3.2, with each body indicated by a separate color. The check valve is shown in Fig. 3.3.

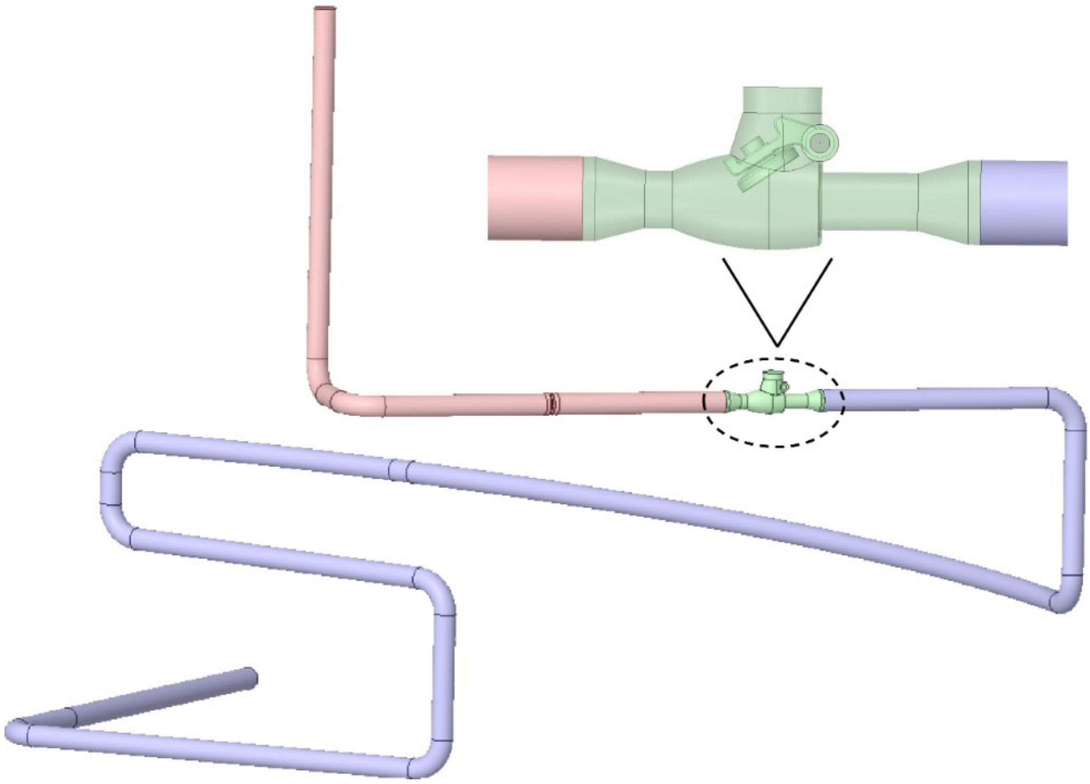

**Figure 3.2:** Overview of the pipe geometry, with the three separate bodies highlighted by color.

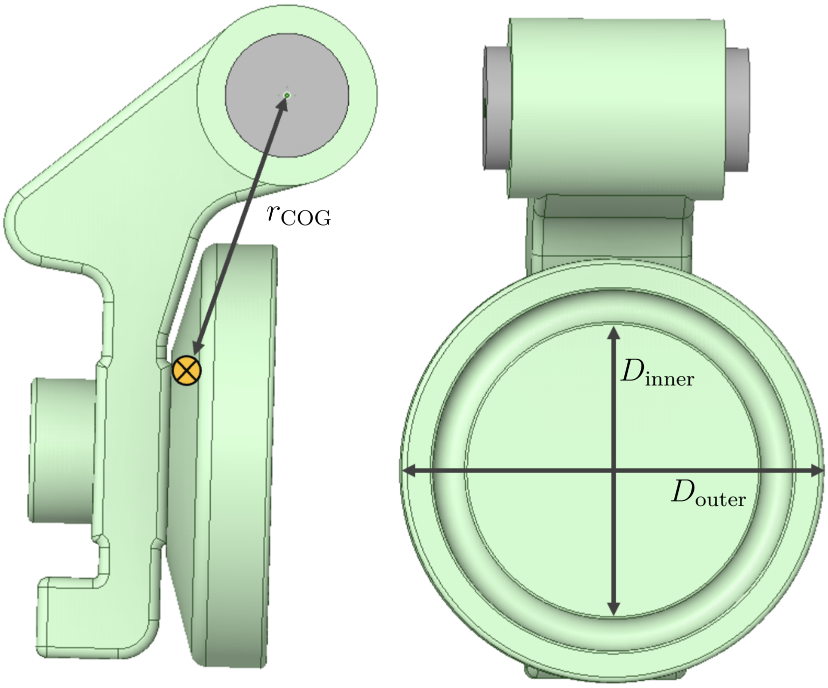


**Figure 3.3:** Geometry of the swing check valve, indicating the distance from the axis of rotation to the center of gravity and the inner and outer disc diameters.

## 3.2 STAR-CCM+ Model Setup

All 3D CFD simulations are performed using STAR-CCM+ [8]. After importing the CAD geometry, surfaces are assigned appropriate boundary names and a Boolean subtract operation is performed to remove the solid check valve from the surrounding volume, leaving only the fluid domain.

Rather than assigning the entire geometry to a single region, two separate regions are created: one enclosing the check valve and one representing the remainder of the pipe. An internal interface is defined between the two regions, allowing them to be meshed independently. This reduces the computational cost during transient simulations involving valve motion, where only the region surrounding the valve requires localized remeshing.

Two main approaches exist in STAR-CCM+ for handling moving solid components within a computational domain: the overset mesh and the morphing mesh techniques. The morphing mesh approach, when combined with a gap closure model and a remeshing model, was selected for the present work as it enables full contact between the valve disc and its surrounding surfaces.

## 3.3 Mesh study

Prior to running transient simulations, a mesh independence study was conducted using steady-state simulations. This study was carried out as part of the simulations used to determine the static torque and loss coefficients, described in Sec. 3.6.1, and was performed with the check valve held fixed at 26° open. The static torque coefficient $C_{HS}$ and the loss coefficient $K$ were selected as convergence metrics, as they are directly relevant to both the primary and secondary objectives of the study. A velocity inlet of 3.5 m/s was applied at the lower pipe end, and a pressure outlet at the upper end. The simulation setup is shown in Fig. 3.4, indicating the location of each boundary condition (BC) relative to the check valve.


**Figure 3.4:** The check valve configuration during the mesh study.

The inlet velocity of 3.5 m/s was adopted from the master's thesis by Giacomo Vavassori (2017) [15], in which torque coefficients were computed using STAR-CCM+ to implement the `th_sr` check valve model in RELAP5.

The segregated flow solver, together with the $k - \varepsilon$ turbulence model, was used for these simulations, as it provided faster convergence at the smaller valve angles considered as part of the broader set of simulations described in Sec. 3.6.1.

Due to the substantial computational cost of the transient simulations, the mesh study was limited to the steady-state case, and full mesh independence of the transient simulations was not verified independently.

# 3.4 Transient simulations

## 3.4.1 Preliminary motion tests

In the first transient simulations, progressively more complex test cases were performed to systematically develop a model capable of handling all relevant features required for the moving check valve simulations.

### Constant rotation

The first test case consists of a prescribed constant rotation of the check valve from the fully open position to fully closed and back, at rotation rates of 10 rad/s to 20 rad/s — sufficient to complete a full cycle in approximately 0.1 s. This test was performed to verify that the morphing mesh, gap closure model, and remeshing model function correctly throughout the full range of valve motion.

A key challenge when combining a morphing mesh with a remeshing model is controlling the frequency of remeshing events. If the mesh morphs too much before remeshing, cell quality deteriorates significantly; however, remeshing too frequently is also undesirable, as the solution must be interpolated onto the new mesh at each remesh event, which can introduce errors in the flow field. The built-in remeshing model in STAR-CCM+ triggers a remesh when cells are projected to reach zero volume or fall below a specified quality threshold at the next time step. While this works well when the valve is close to a wall — where boundary layer cells compress rapidly — cell quality can degrade significantly before the condition is met when the valve is further from the wall, making this approach unreliable on its own.

To address this, a forced remeshing event was implemented in the Simulation Operations, triggering a remesh whenever the valve has rotated by a fixed angular increment $\Delta\theta_{\text{mesh}}$. After each remesh, the event resets and the simulation continues from the next time step. This approach ensures consistent mesh quality throughout the valve motion regardless of proximity to the wall. The implementation and a flowchart of the logic are shown in Fig. 3.5.

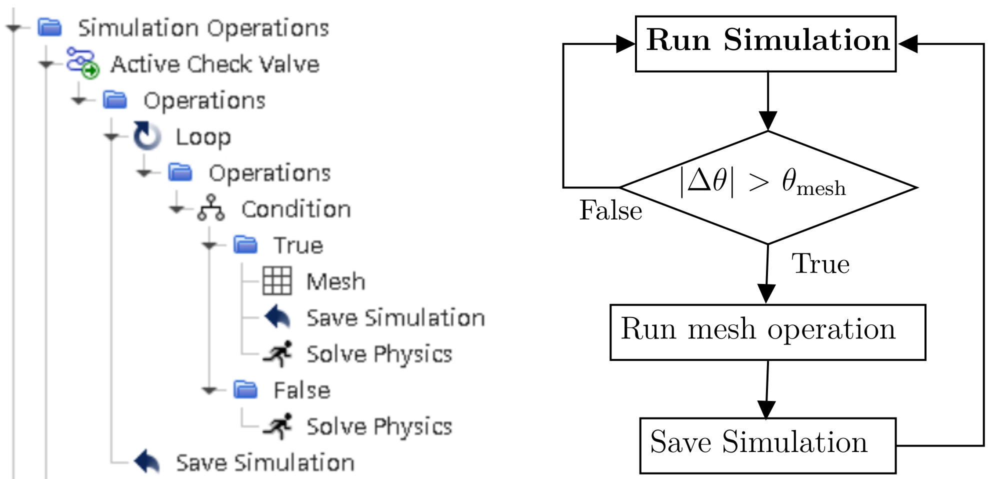


**Figure 3.5:** Morphing mesh logic.

Results from the constant rotation case are not included in this report, as this test serves only as an intermediate step in the development of the final simulation model.

#### Drop test

Once the constant rotation case had been deemed successful, a drop test simulation was performed. In this case, the check valve was released in a quiescent flow from the fully open position and allowed to close under the influence of gravity. The purpose of this test is to ensure that the model correctly handles motion induced by physical forces, and the results are verified against an analytical solution of an equivalent 1D pendulum model (Appendix A).

This test also serves additional purposes: it reveals fundamental differences between the torques acting on the body in the 3D and 1D models due to implicit effects, and it provides an opportunity to evaluate the time-step sensitivity of the valve motion in the absence of significant fluid forces.

In STAR-CCM+, this requires updating the model from a morphing mesh approach to a DFBI morphing model. The DFBI model requires specification of the valve mass, the initial center of mass coordinates, and its moment of inertia components, as described in Sec. 2.2.3.1.

## 3.5 Complete STAR-CCM+ Model & Force-based RELAP5 Model

With the preliminary validation cases completed, the CFD model was ready for transient simulations comparing the dynamic behavior of the swing check valve during sudden pressure transients between the 3D CFD and 1D RELAP5 models. The work described in the following subsections was conducted iteratively, with sensitivity studies performed in parallel, and does not necessarily reflect the chronological order of the project.

Each simulation performed in STAR-CCM+ was also carried out using the corresponding RELAP5 model, which represents an equivalent piping network in a 1D framework. Minor geometric differences exist between the two models, as shown in Fig. 3.6. The check valve is positioned 0.203 m closer to the fluctuating pressure BC, and the total pipe length in the RELAP5 model is slightly longer than in STAR-CCM+.

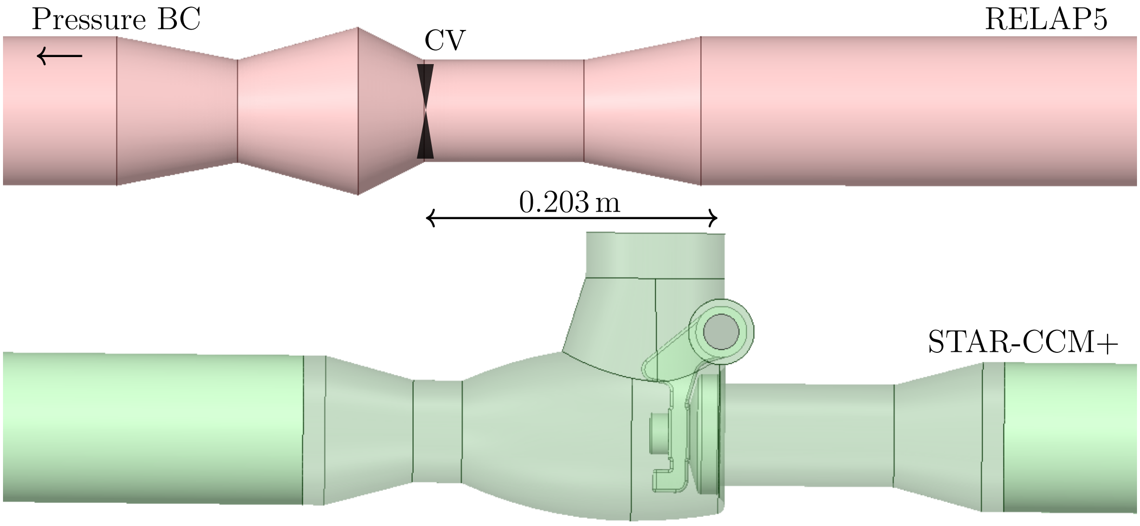


**Figure 3.6:** Differences in the check valve housing geometry between the RELAP5 and STAR-CCM+ models, including cross-sectional area variation and valve positioning. In RELAP5, the check valve (CV) is positioned 0.203 m closer to the pressure BC than in STAR-CCM+.

The difference in pipe length and check valve position is expected to have only a minor influence on the results, primarily introducing a small shift in wave arrival times. The difference in housing geometry may have a larger effect, as the local area expansion and contraction around the check valve influence the flow resistance and pressure distribution near the valve.

### 3.5.1 Pressure Wave with Open Valve

The open valve case captures a pressure transient propagating through the pipe while the check valve is held in the fully open position, as shown in Fig. 3.7.

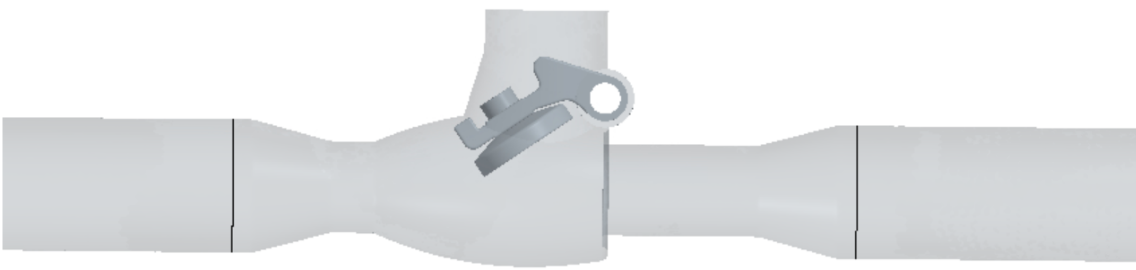

**Figure 3.7:** Valve configuration for the fully open valve case.

The transient simulation was initialized from a steady-state solution to ensure a physically consistent flow field prior to the introduction of the pressure transient. The absolute pressure field at the start of the simulation is shown in Fig. 3.8, which accounts for the reference pressure, gauge pressure, and hydrostatic pressure. The pressure in the analysis is set higher than the actual system pressure to prevent the formation of a vacuum when the pressure wave reflects. This elevated pressure was used in all subsequent simulations in both STAR-CCM+ and RELAP5.

The end of the pipe at the lowest elevation was assigned a wall BC, representing a closed valve at that location.

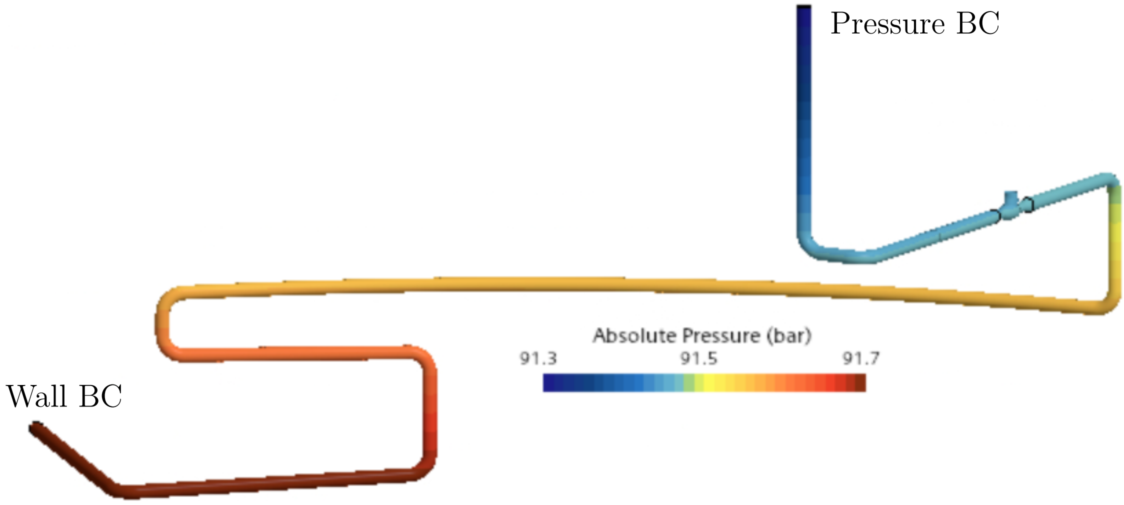


**Figure 3.8:** Absolute pressure field at the start of the open valve simulation.

Once a steady state was reached, the pressure BC was updated to a prescribed time-varying pressure, representing the disturbance generated by a sudden pressure drop event in an adjacent section of the piping system. This fluctuating pressure was extracted from RELAP5 simulations and applied identically in both models to ensure consistency.

To compare the 3D and 1D model results, pressure and mass flow rate were monitored at several locations along the pipe at comparable distances from the pressure BC.

Both the coupled and segregated flow solvers were evaluated using the $k$-$\omega$ SST turbulence model. As discussed in Sec. 2.2.2, the coupled solver was expected to perform better for pressure wave propagation problems. No major differences were observed between the two solvers (Appendix B), though the coupled solver showed slightly closer agreement with RELAP5 and was therefore selected for all subsequent transient simulations. Only results obtained with the coupled solver are presented in this report.

All transient simulations used the IAPWS-IF97 water model (International Association for the Properties of Water and Steam, Industrial Formulation 1997), which accounts for compressibility effects [8].

### 3.5.2 Pressure Wave with Active Valve

Building on the open valve case, valve motion was introduced to allow the check valve to respond dynamically to the transient flow field generated by the same pressure

BC as in the open case. Starting from the fully closed position, shown along with the mesh in Fig. 3.9, the valve was free to open and close in response to the pressure forces acting on it.

As in the previous case, a steady-state simulation was performed prior to the transient analysis. Achieving convergence proved significantly more challenging than in the open valve case. As shown in Fig. 3.9, the gap closure model deactivates all cells connecting the two sides of the pipe across the check valve when it is closed. The fluid on the front side of the check valve is thereby isolated from the pressure BC, effectively leaving it enclosed between two wall boundaries.

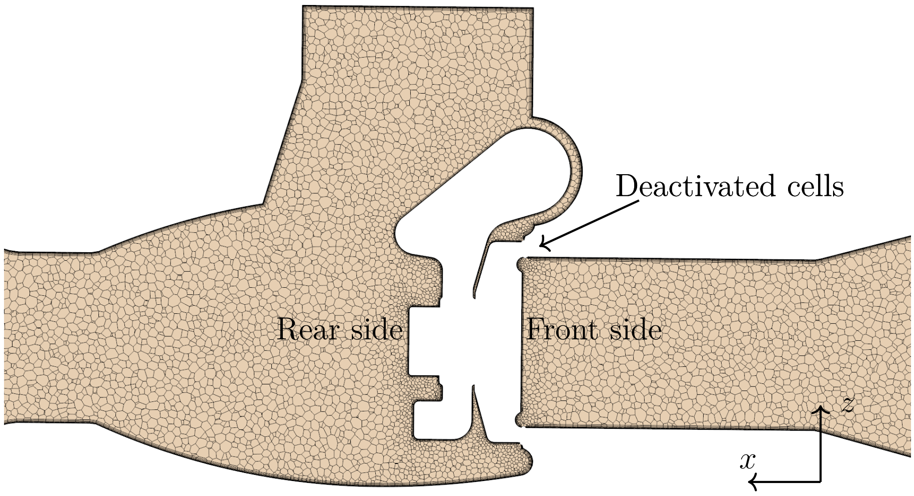


**Figure 3.9:** Initial configuration for the active valve case, showing the mesh with cells deactivated by the gap closure model and the coordinate system sign convention.

The gap closure model introduced an additional complication. Even when the pressure was equalized on both sides of the check valve, a large closing force was reported. This arose because the gap closure model deactivates cells on the front face of the check valve without compensating for the reduction in surface area. As a result, the DFBI model computed the net force from unequal areas on the two sides of the disc, $A_{\text{front}} \neq A_{\text{rear}}$, such that even at equal pressure $P$:

$$F_x = P \cdot A_{\text{rear}} - P \cdot A_{\text{front}} \neq 0 \tag{3.1}$$

To correct for this, a user-defined force was implemented to replace the DFBI force while the check valve remained close enough to the seat for cells to be deactivated. The user-defined force was computed from the surface-averaged pressure on the front and rear faces of the disc:

$$\mathbf{F}_h = \left(\bar{P}_{\text{rear}} - \bar{P}_{\text{front}}\right) \mathbf{A}_{\text{disc}} \tag{3.2}$$

Once all deactivated cells were reactivated, the force switched back to the built-in DFBI formulation, as expressed in Eq. (2.11).

To ensure consistency between the two models, the input parameters of the RELAP5 model — including mass, moment of inertia, and the geometric parameters shown in Fig. 2.1 — were extracted directly from the STAR-CCM+ model. The loss coefficient is an additional input parameter, obtained from steady-state CFD simulations as described in Sec. 3.6.1.

## 3.6 `th_sr` RELAP5 Model

With the primary objective established, attention now turns to the secondary objective along the dashed lines in the workflow chart (Fig. 3.1): implementing the `th_sr` check valve model in RELAP5.

This model requires two sets of tabulated input parameters: the static torque coefficient $C_{HS}(\theta_i)$ in Eq. (2.20), obtained at a number of discrete valve angles $\theta_i$ from steady-state simulations, and the coefficients $k_{1-6}$ in Eq. (2.22), determined from transient simulations and likewise tabulated as functions of the valve angle, $k_{1-6}(\theta_i)$.

The implementation approach follows that of Giacomo Vavassori's 2017 master's thesis, "Swing Check Valve Characterization: 3D CFD Validation of One-Dimensional Models Used in RELAP5" [15], where the same model was applied. However, since the model coefficients are case-specific and require tuning, the parameter values obtained in his work cannot be directly transferred to the present model.

A third parameter of interest is the loss coefficient $K$, described in Sec. 2.3.3. This coefficient can be evaluated from the same simulations used to determine the static torque coefficients.

### 3.6.1 Loss Coefficients and Static Torque Coefficients

The loss and static torque coefficients were obtained from steady-state simulations, with a velocity inlet at one end of the pipe and a pressure outlet at the other, set to a value corresponding to normal system operation. As $C_{HS}$ is required as a function of valve angle (see Sec. 3.6.2), simulations were performed at 19 valve angles between 56° (fully open) and 2° for both the forward and backward axial flow directions past the check valve. Starting with the valve fully open, each simulation was run to convergence, after which the valve was rotated to the next angle and the simulation continued from this state. The BCs for each flow direction, along with the measurement locations used to determine the loss coefficient, are indicated in Fig. 3.10.

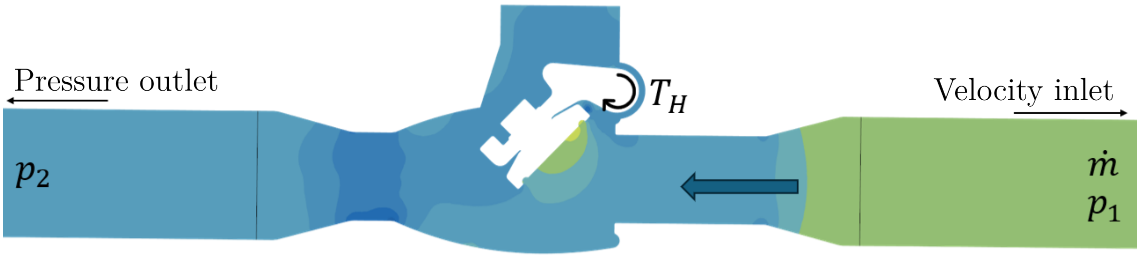


**(a)** Forward flow velocity


**(b)** Backward flow velocity

**Figure 3.10:** Pressure contour plot showing the BCs and measurement locations used for the loss coefficient determination, along with the torque sign convention.

Vavassori investigated the Reynolds number dependency of the static torque coefficient. When a gravity model was included in the physics setup, the results showed that for slow flow velocities, $C_{HS}$ varies significantly when the check valve is near its fully open position, but only negligibly when near its closed position. His investigation concluded that a velocity of 3.5 m/s proved sufficiently high to guarantee good results, and for that reason the same value was adopted in this work [15].

The mesh convergence study described in Sec. 3.3 was performed during the extraction of these coefficients.

### 3.6.2 Rotational Torque Coefficients

Since Eq. (2.21) requires $\tau_{HS}$, this quantity must be known for any valve angle $\theta$ and flow direction the check valve may encounter. Using the $C_{HS}$ values obtained from the steady-state simulations, continuous functions $C_{HS}^{+}(\theta)$ and $C_{HS}^{-}(\theta)$ are obtained from curve fitting for forward and backward flow, respectively.

The inlet velocity ($V_{in}$) and check valve angular velocity ($\dot{\theta}$) are monitored and stored throughout the transient simulations in order to determine the coefficients $k_{1-6}$ in the regression model $\bar{C}_{HR}$.

The input parameters for the `th_sr` model thus consist of tables of $C_{HS}(\theta_i)$ and $k_{1-6}(\theta_i)$ for $\theta_i \in [-\theta_{max}, \theta_{max}]$, where the sign of the angle corresponds to the direction of the flow. The regression model coefficients are computed using a MATLAB script based on one developed by Vavassori [15] and can be found in Appendix C.

To collect sufficient data for fitting the regression model $\bar{C}_{HR}$, 9 transient simulations were performed, covering inlet velocity and angular velocity combinations representative of the check valve's actual operating conditions. Each simulation was run until the check valve had rotated from fully open to fully closed, or vice versa.

The BCs for each case are listed in Table 3.1, where $\dot{\theta}_{pre}$ denotes the angular velocity prescribed to the check valve and $\dot{V}_{in}$ denotes the rate of change of inlet velocity.

| Case | $V_{in}(t=0)$ [m/s] | $\dot{V}_{in}$ [m/s$^2$] | $\dot{\theta}_{\mathrm{pre}}[rad/s]$ |
|---|---|---|---|
| 1 | 3.5 | $-100$ | 0 |
| 2 | 3.5 | $-600$ | 0 |
| 3 | 3.5 | 0 | 10 |
| 4 | 3.5 | 0 | 20 |
| 5 | 3.5 | $-50$ | 10 |
| 6 | 3.5 | $-200$ | 10 |
| 7 (drop test) | 0 | 0 | 0 |
| 8 | 0 | 35 | 0 |
| 9 | $-3.5$ | 0 | 0 |

**Table 3.1:** BCs for the nine transient simulations used to determine the rotational torque coefficients.

The negative initial velocity in Case 9 refers to a backward flow direction. The check valve is started fully open in all cases except Case 8, where it begins fully closed. The fluid in these simulations was modeled as water with constant density, in order to avoid compressibility effects influencing the check valve motion.

# 4

# Results and Discussion

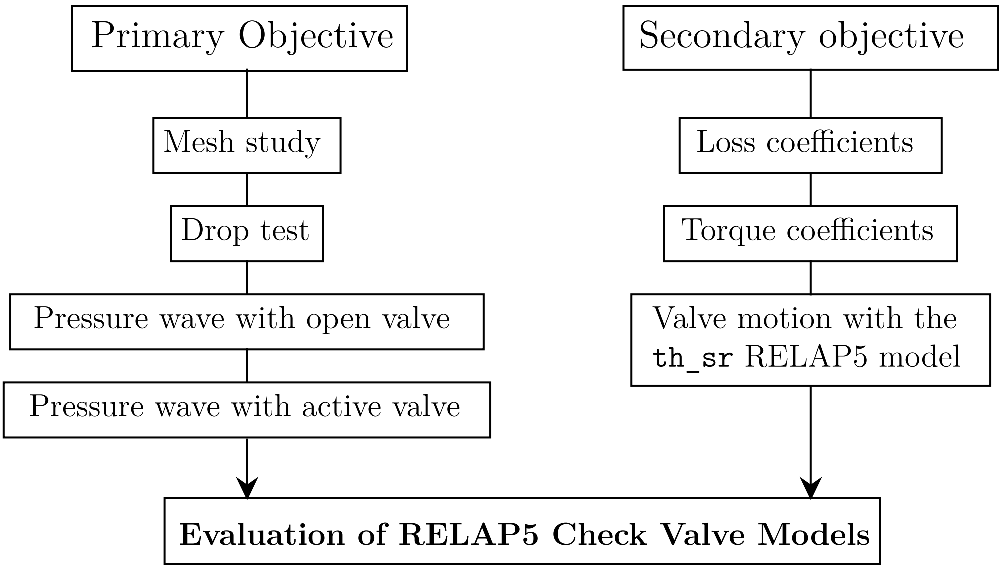


The order of the results is based on the thesis workflow chart, Fig. 3.1. The results related to the primary objective are presented first, followed by those related to the secondary objective.

## 4.1 Mesh Study

The mesh independence study was conducted as described in Sec. 3.3, with the check valve fixed at $\theta = 26°$. The results are summarized in Table 4.1.

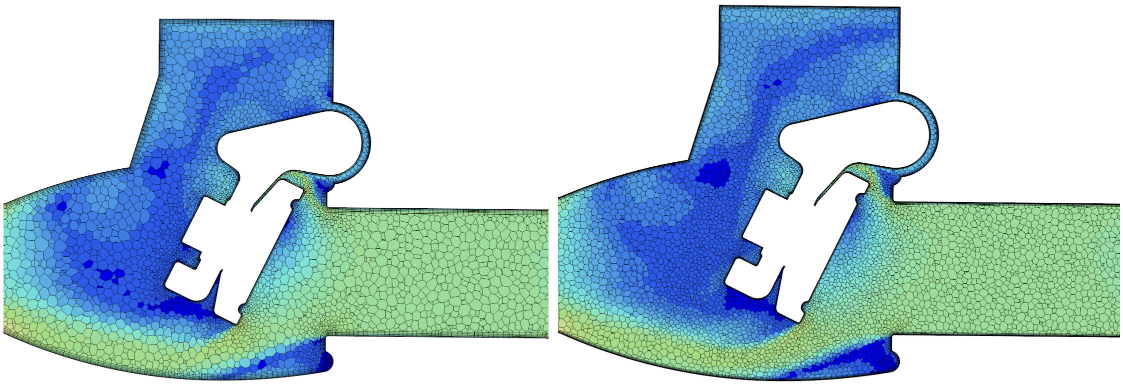

**(a)** Coarse mesh **(b)** Medium mesh

**Figure 4.1:** Comparison between coarse and medium mesh configurations near the check valve.

**Table 4.1:** Mesh convergence study for the CFD simulations.

| Mesh | Cells [-] | $C_{HS}$ [-] | $\Delta C_{HS}$ [%] | $K$ [-] | $\Delta K$ [%] | CPU time [h] |
|---|---|---|---|---|---|---|
| Coarse | 1 696 491 | 4.449 | – | 5.278 | – | 16.6 |
| Medium | 1 948 980 | 4.497 | 1.08 | 5.254 | 0.45 | 21.7 |
| Fine | 2 345 522 | 4.558 | 1.36 | 5.308 | 1.03 | 24.6 |

The predicted values of $C_{HS}$ and $K$ agree to within 2.5% of each other, indicating a mesh-independent solution. The relative changes are small enough to conclude that further refinement beyond the medium mesh yields negligible gains in accuracy at the cost of a 13% increase in CPU time. The medium mesh was therefore selected for all subsequent simulations. Minor adjustments to the mesh were made to accommodate the morphing mesh required for the active valve simulations, while maintaining a comparable cell count and level of refinement.

The wall $y^+$ distribution for all three meshes is shown in Fig. 4.2. Values fall predominantly in the range $6 \leq y^+ \leq 72$, though the coarse mesh exhibits a distribution slightly skewed toward higher values.

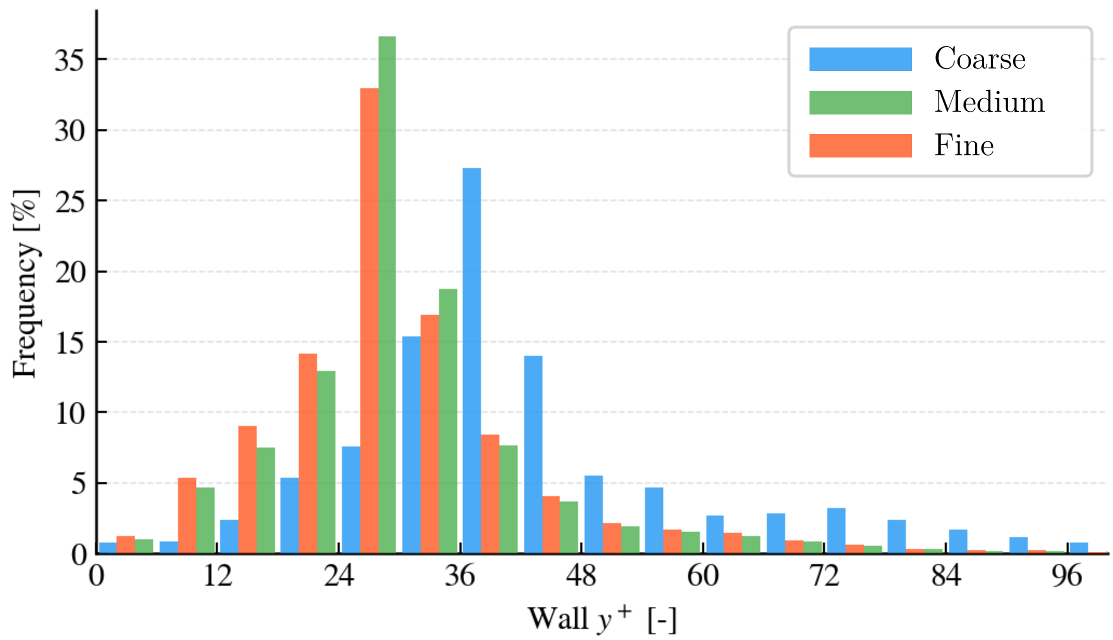


**Figure 4.2:** Histogram plot showing the distribution of wall $y^+$ values for the different meshes.

## 4.2 Drop Test

Drop tests were performed to validate the DFBI model in STAR-CCM+ against a 1D reference code (Appendix A). Figure 4.3 compares the angular trajectory and net torque of the free-falling swing check valve between the two models.

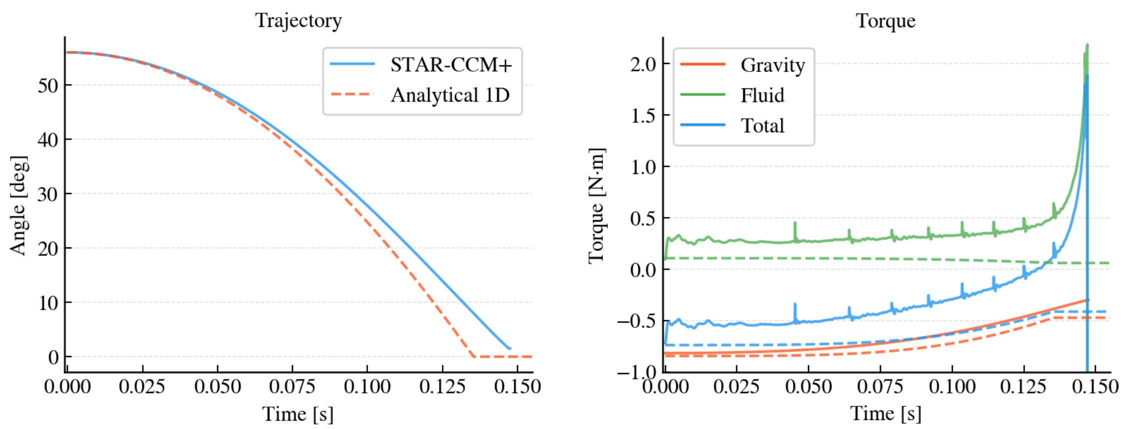


**Figure 4.3:** Comparison of the DFBI simulation results (solid lines) against the 1D reference code (dashed lines) for the free-falling swing check valve: angular trajectory (left) and net torque driving the motion (right).

The trajectories show close agreement during the early descent, though the 1D model predicts a steeper decline and earlier seating. The torques reveal these effects more clearly: the fluid torque in STAR-CCM+ initially coincides with the 1D buoyancy estimate, but increases by approximately $0.15\,\mathrm{N\,m}$ once the valve begins to move, suggesting that the effective lever arm shifts from the center of gravity to the center of pressure as the pressure distribution develops. The fluid torque continues to increase throughout the descent — contrary to the 1D buoyancy torque, which decreases as the moment arm shortens — consistent with a growing added mass contribution as the valve accelerates. At approximately $t = 0.14\,\mathrm{s}$, the total torque changes sign as hydrodynamic damping begins to decelerate the closing motion, an effect absent from the 1D model.

The periodic discontinuities in the STAR-CCM+ torque curve are numerical artifacts caused by remeshing events at every $\Delta\theta = 6^\circ$ of valve rotation, and do not measurably affect the trajectory.

The drop test confirms that the DFBI model captures physical effects such as added mass and hydrodynamic damping that are absent from simplified 1D formulations, and demonstrates that these effects have a meaningful influence on the overall motion of the check valve.

Three time-step sizes were evaluated for the drop test: $\Delta t$ = 100, 50, and 10 $\mu$s. No significant difference in the valve trajectory was observed between the cases, confirming that the solution is insensitive to the time-step size within this range.

## 4.3 Pressure Wave with Open Valve

To validate the pressure wave propagation in STAR-CCM+, the check valve was held in the fully open position while a pressure transient was generated by a fluctuating pressure BC. Two probes were placed along the pipe axis with an axial separation of $\Delta x = 0.62L$, where $L$ is the total pipe length, as shown in Fig. 4.4.

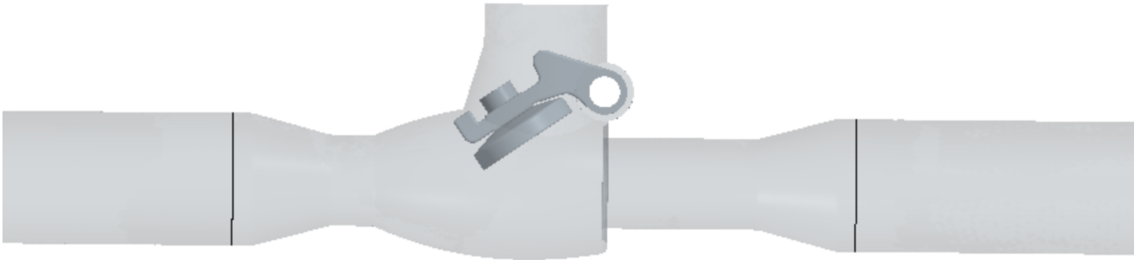

**(a)** Valve configuration.

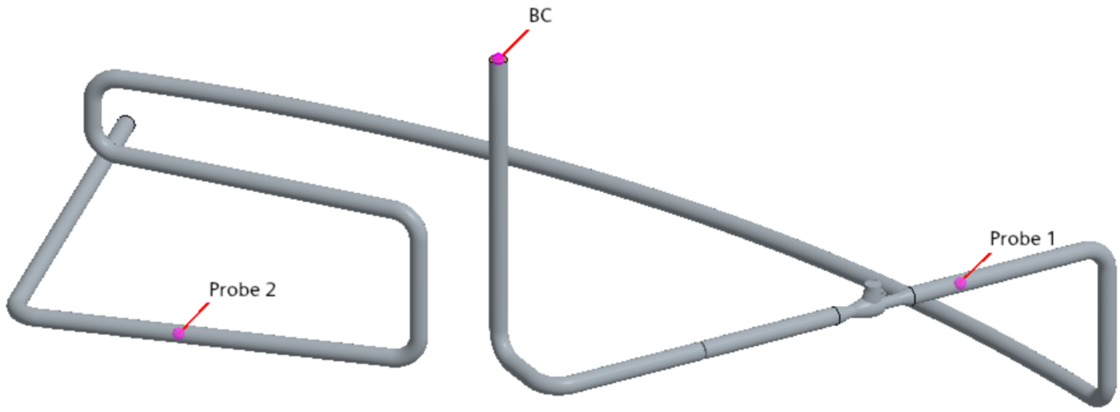


**(b)** Positions of the measurement probes.

**Figure 4.4:** Simulation setup for the stationary valve case.

Figure 4.5 shows the pressure and mass flow rate at both probe locations for STAR-CCM+ and RELAP5. The frequency and amplitude of the pressure wave are well captured by both models, with coefficients of determination of $R^2 = 0.9360$ and $R^2 = 0.9789$ at Probe 1 and Probe 2, respectively. The mass flow rate shows similarly strong agreement, with $R^2 = 0.9757$ at Probe 1 and $R^2 = 0.8287$ at Probe 2. The oscillation amplitudes decay faster in RELAP5 than in STAR-CCM+ as the simulation progresses. This can be attributed to differences in surface friction between the two models: in STAR-CCM+, the walls are set to hydraulically smooth, whereas a roughness height is specified in RELAP5. Given this smooth-wall setup in STAR-CCM+, the observed decay is thereby mainly a byproduct of numerical dissipation rather than physical wall friction.

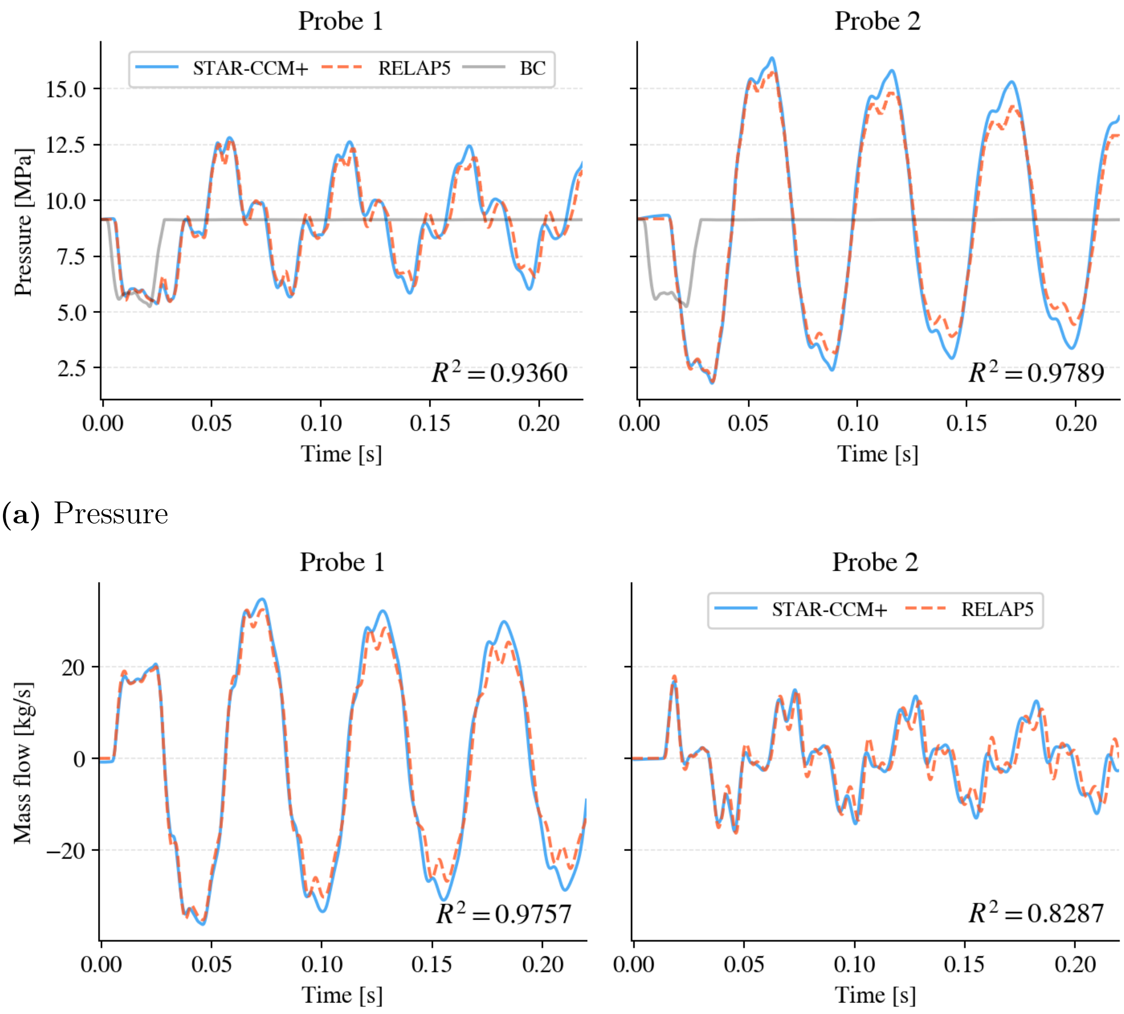


**(a)** Pressure



**(b)** Mass flow rate

**Figure 4.5:** Comparison of pressure and mass flow rate between STAR-CCM+ and RELAP5 at Probe 1 and Probe 2.

The loss coefficient for the fully open valve configuration is verified against the RELAP5 model by comparing the pressure drop and mass flow rate. The results are shown in Fig. 4.6.

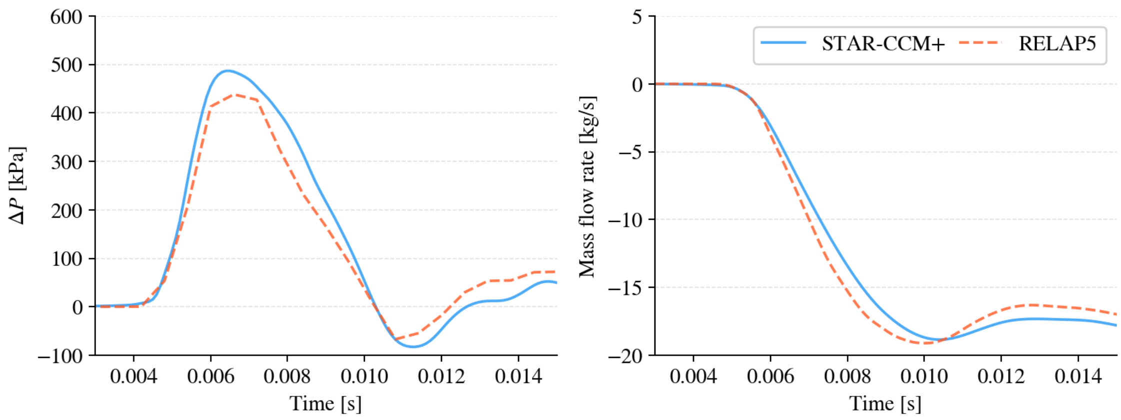


**Figure 4.6:** Pressure drop and mass flow rate at the loss coefficient measurement locations (Fig. 3.10a) for the fully open valve case.

The close agreement between the two curves is an expected result, given that the loss coefficient input in RELAP5 was obtained from STAR-CCM+ simulations of the fully open valve configuration. It nonetheless serves as an important verification and will be relevant for the upcoming analysis.

As shown in Fig. 4.7, the pressure wave arrives at Probe 2 with a delay relative to Probe 1, from which the speed of sound can be estimated as $c = \Delta x/\Delta t = 1540.2\,\mathrm{m/s}$. This value agrees with the National Institute of Standards and Technology (NIST) reference for water at 7.5 MPa and 50 °C to within 1% [17], and can be seen as a complementary validation of the chosen material model.

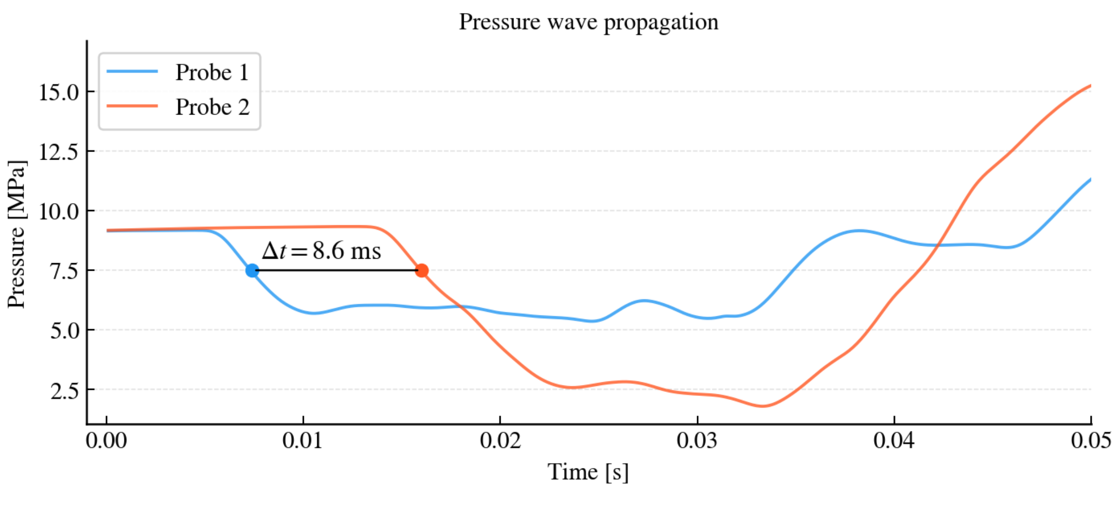


**Figure 4.7:** Pressure histories at Probe 1 and Probe 2, with the arrow indicating the wave propagation delay $\Delta t$ between the two locations.

The simulation covered 0.22 s of physical time at a computational cost of 1614 CPU hours.

## 4.4 Pressure Wave with Active Valve

Before presenting the results, a note on the time-step size is warranted. It will be seen in the plots that there is a delay between the quantities predicted by STAR-CCM+ relative to RELAP5, which is a consequence of time-step sensitivity. For the simulations, time-step sizes ranging from 2 to 50 $\mu$s were evaluated. It was found that the larger time steps cause both the valve opening and other flow quantities to occur later, whereas when the time step was equal to or smaller than that used by RELAP5 ($\Delta t = 6\ \mu$s), the valve opening occurred at the same time as predicted by RELAP5. Despite this sensitivity, the effect on the overall valve motion was minor. For the longer simulations, an adaptive time step ranging from 10 to 50 $\mu$s was therefore adopted to balance accuracy and computational cost. The benefit is substantial: simulating 0.3 s required approximately 1923 CPU hours with the adaptive scheme, compared to 1161 CPU hours for only 0.011 s with a fixed time step of 2 $\mu$s — a factor of roughly 16.5 in computational efficiency. The effect of time-step size on the valve opening and mass flow oscillations is included in Appendix D, and all results presented in this section are from simulations using the adaptive time step, unless otherwise stated.

### 4.4.1 Valve motion

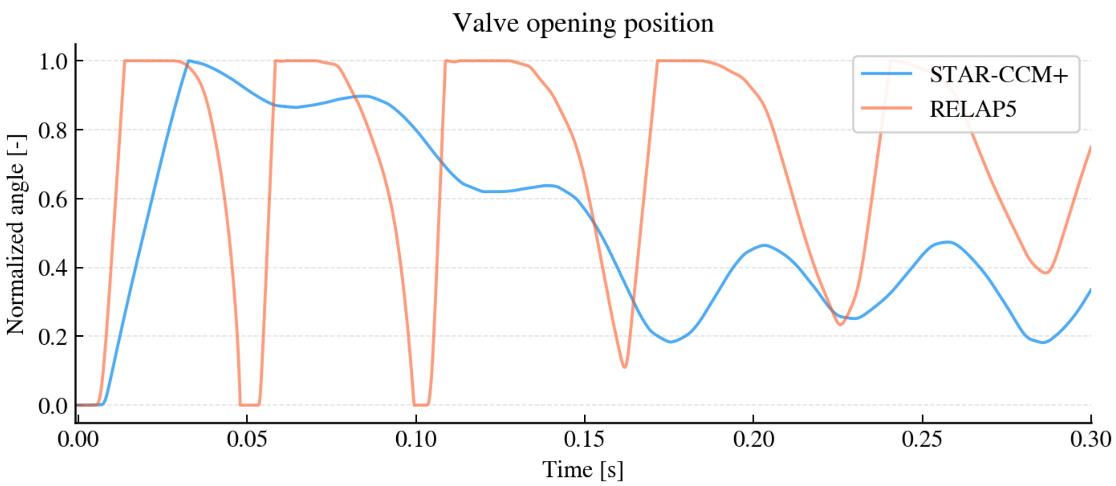


**Figure 4.8:** Comparison of normalized valve opening angle between STAR-CCM+ and RELAP5 over the full simulation duration.

The valve trajectories predicted by STAR-CCM+ and RELAP5 are compared in Fig. 4.8. RELAP5 predicts significantly faster valve motion: the check valve has nearly completed a full open-close cycle before STAR-CCM+ even predicts full opening. This behavior is further illustrated in Fig. 4.9, where the RELAP5 check valve fully opens and closes during the first two mass flow oscillations, while the STAR-CCM+ check valve responds more gradually and does not fully close during flow reversal.

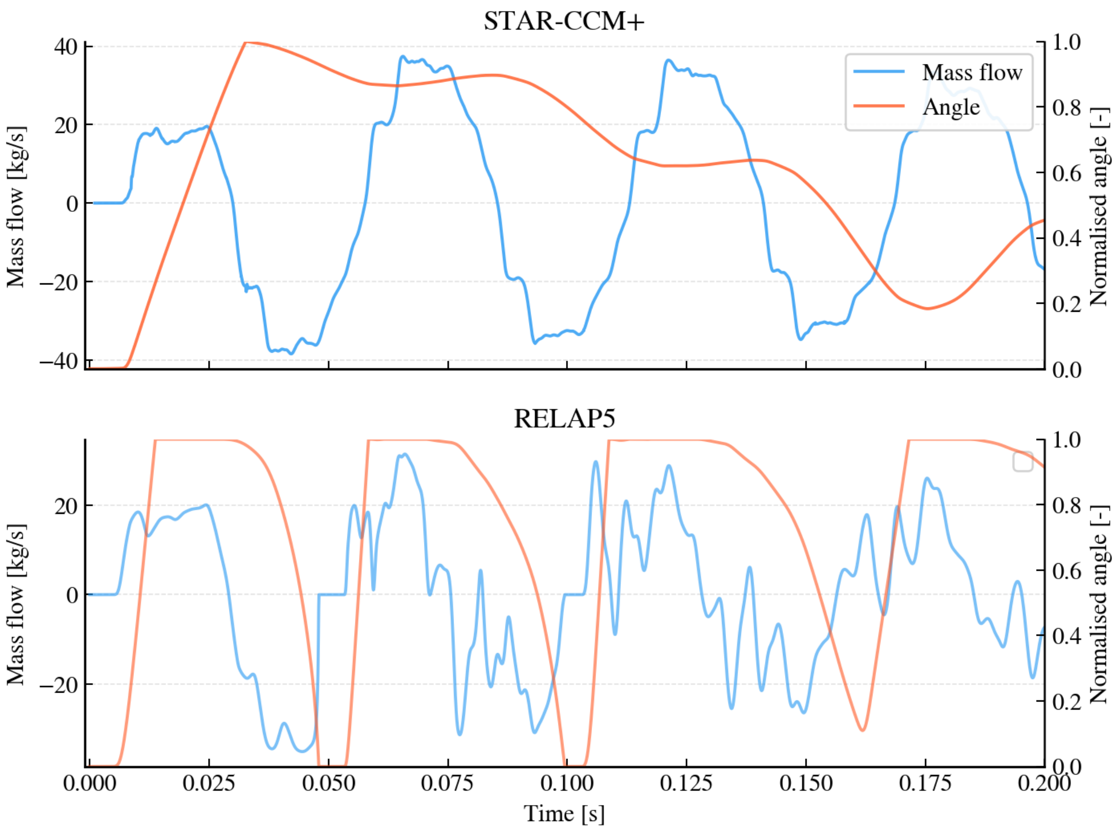


**Figure 4.9:** Normalized valve opening angle and mass flow rate for STAR-CCM+ and RELAP5, illustrating the correlation between flow oscillations and valve response.

The following subsections investigate the main factors contributing to the discrepancy between the two models.

### 4.4.2 Added Mass Inertia

The effective inertia of the check valve is underestimated in the 1D model due to the absence of added mass and other hydrodynamic effects, which are naturally captured by the 3D CFD model. This is supported by STAR-CCM+ simulations in which the check valve density — and consequently its moment of inertia — was reduced by 50%, showing no significant change in the valve trajectory (Appendix E). This suggests that the mechanical moment of inertia plays a minor role in the dynamics, and that the dominant inertial contribution stems from the surrounding fluid rather than the solid body.

### 4.4.3 Pressure Differential and Force Formulation

The faster valve opening predicted by RELAP5 is primarily driven by a larger predicted pressure differential $\Delta p$ across the disc, producing a greater net torque. As shown in Fig. 4.10, RELAP5 exhibits consistently larger $\Delta p$ throughout the simulation, while the STAR-CCM+ value remains low following the initial rise. Sharp discontinuities appear when the check valve contacts a surface: in STAR-CCM+ at $t = 0.033\,\mathrm{s}$ upon contact with the top surface, and in RELAP5 each time the valve closes against the seat.

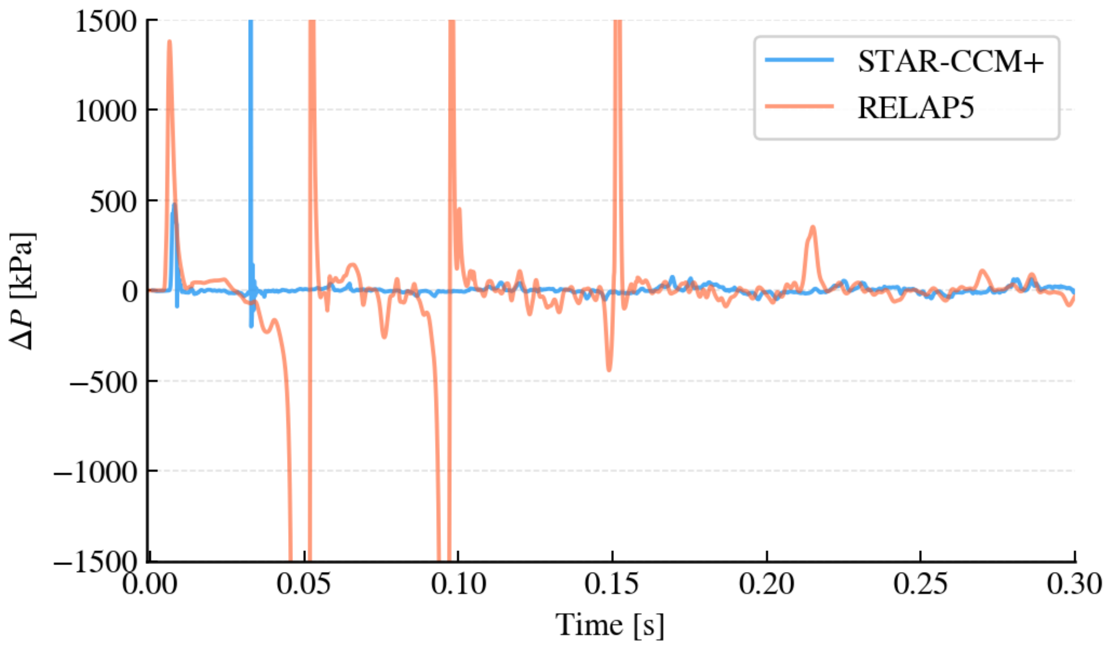


**Figure 4.10:** Pressure differential across the check valve disc for STAR-CCM+ and RELAP5 over the full simulation. The $y$-axis is clipped for readability; peak values in RELAP5 reach approximately 5800 kPa.

To isolate the contribution of the force formulation, the RELAP5 formulation was reproduced in STAR-CCM+ using pressure probes at equivalent axial positions (see Appendix F). As shown in Fig. 4.11, the result exceeds the DFBI integrated surface force, confirming that the formulation itself contributes to the overestimation independently of the pressure field.

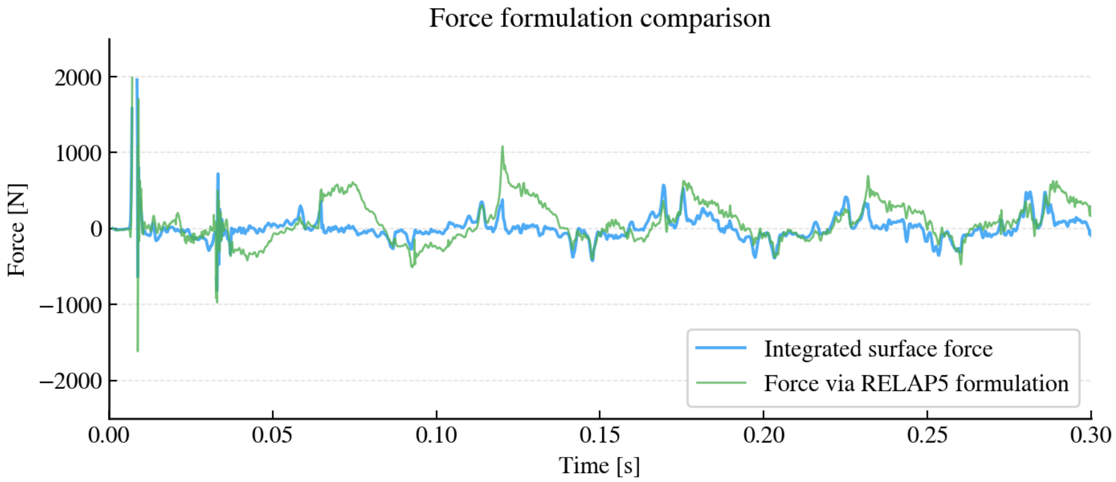


**Figure 4.11:** Comparison between the integrated surface force from STAR-CCM+ and the RELAP5 force formulation reproduced in STAR-CCM+ using axially displaced pressure probes.

In the RELAP5 formulation, the pressure is evaluated at fixed axial probe positions rather than on the disc faces, and the projected disc area is assumed constant regardless of opening angle. Multiplying the RELAP5 hydraulic force by $\cos\theta$ is one way to address these shortcomings by scaling the force according to check valve angle, mitigating the overestimation that is especially prominent at large opening angles. The result is shown in Fig. 4.12, covering the first 0.15 s of the simulation.

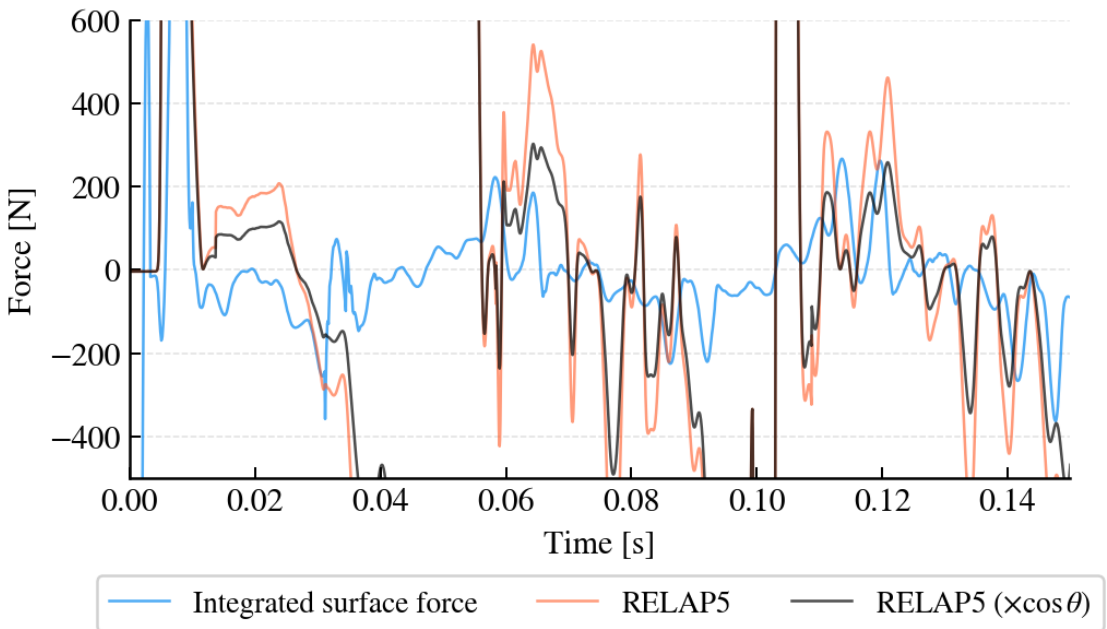


**Figure 4.12:** Comparison of the integrated surface force from STAR-CCM+, the RELAP5 force, and the geometrically scaled RELAP5 force $F_h \times \cos\theta$, accounting for the reduction in projected disc area with valve opening angle.

The scaling reduces the peak force values, bringing them closer to the STAR-CCM+ integrated force, although a residual overestimation remains.

### 4.4.4 Loss Coefficient Discrepancy

The most significant difference between the two models occurs during the initial pressure rise. RELAP5 predicts an initial $\Delta p$ nearly three times as large as STAR-CCM+, which drives the check valve to its fully open position before the flow reverses. The smaller $\Delta p$ combined with the greater effective inertia in STAR-CCM+ means the valve has not fully opened when the flow reverses, and consequently retains a positive angular velocity that must first decelerate to zero before closing can begin.

The relationship between mass flow rate, pressure differential and check valve opening angle is illustrated in Fig. 4.13. In STAR-CCM+, significant mass flow develops much earlier in the opening process: at an angle of 5° ($t \approx 0.0098$ s), the mass flow rate through the check valve is approximately 13.9 kg/s. At the same opening angle in RELAP5 ($t \approx 0.0073$ s), the mass flow rate is only 9.2 kg/s, despite the larger pressure differential. This points to a potential deviation in the loss coefficient at intermediate opening angles as a source of the larger pressure drop in RELAP5.

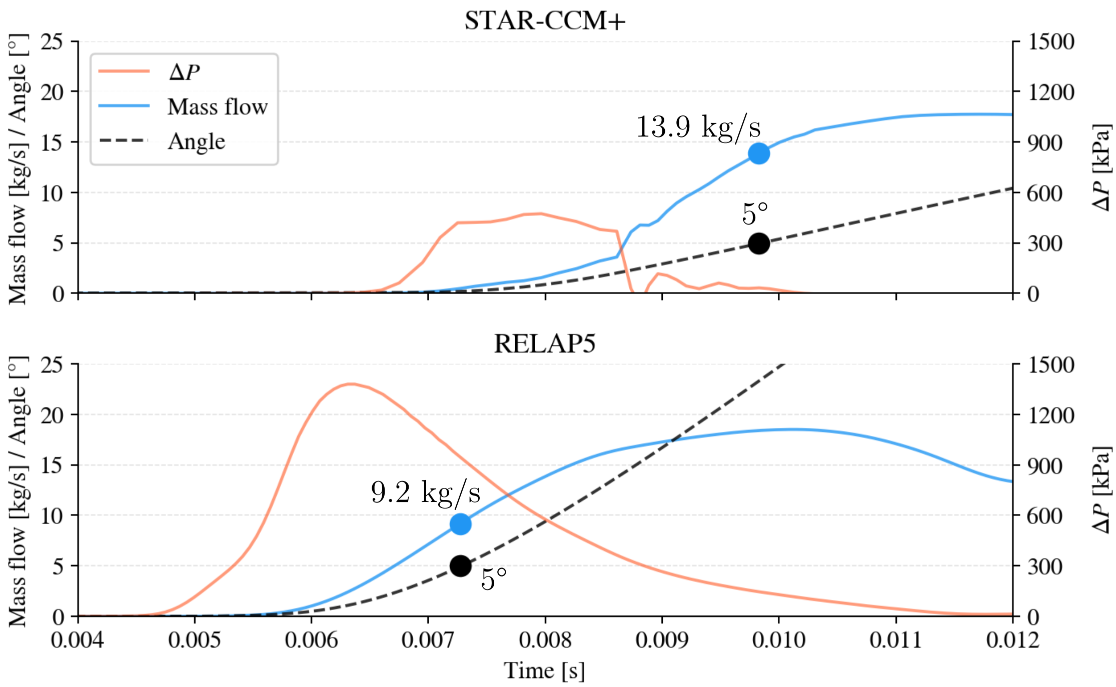


**Figure 4.13:** Evolution of $\Delta p$, mass flow rate, and valve opening angle during the initial opening phase for STAR-CCM+ and RELAP5.

In STAR-CCM+, the sudden increase in mass flow visible at $t \approx 0.0086$ s occurs when the check valve fully separates from its seat and the gap closure model reactivates the previously deactivated cells; pressure contour plots illustrating this process are shown in Appendix G.

To isolate whether a deviation in the loss coefficient between STAR-CCM+ and RELAP5 is responsible for the larger pressure drop in RELAP5, the check valve was fixed at 20% of its fully open position and subjected to the same pressure transient (Fig. 4.14).

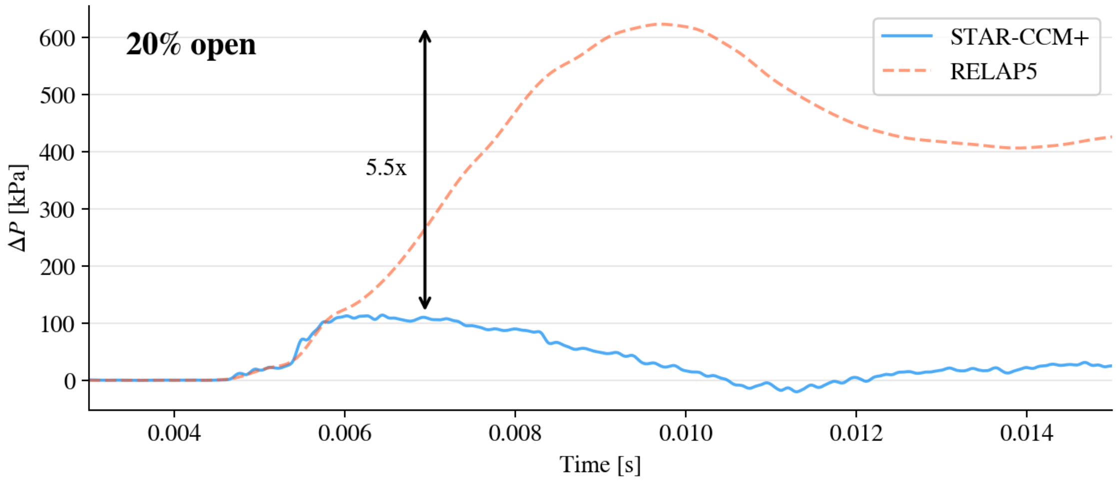


**Figure 4.14:** Pressure drop across the check valve disc for STAR-CCM+ and RELAP5 with the valve fixed at 20% of its fully open position, subjected to the same pressure transient as the active valve case. The arrow indicates the ratio of peak $\Delta p$ between the two models.

The difference in predicted $\Delta p$ is substantial: RELAP5 predicts a peak value approximately 5.5 times larger than STAR-CCM+, and the overall shape of the pressure curve also differs markedly between the two models. In contrast, the two models agree closely when the valve is fixed in the fully open position (Fig. 4.6). Together, these results confirm that the empirical correlation used by RELAP5 to scale $K$ to intermediate opening angles overestimates the flow resistance compared to the 3D CFD model, and that this is a key factor in the discrepancy between the two models.

### 4.4.5 Wave Reflections

Further differences between the models are evident in the pressure evolution at probes placed progressively closer to the check valve, shown in Fig. 4.15.[1] In each plot, the leftmost curve corresponds to the probe nearest the BC, while the rightmost corresponds to the probe closest to the check valve.

[1]The STAR-CCM+ curves were obtained using a short time step and are therefore not affected by the time-step-induced delay discussed in Sec. 4.4.

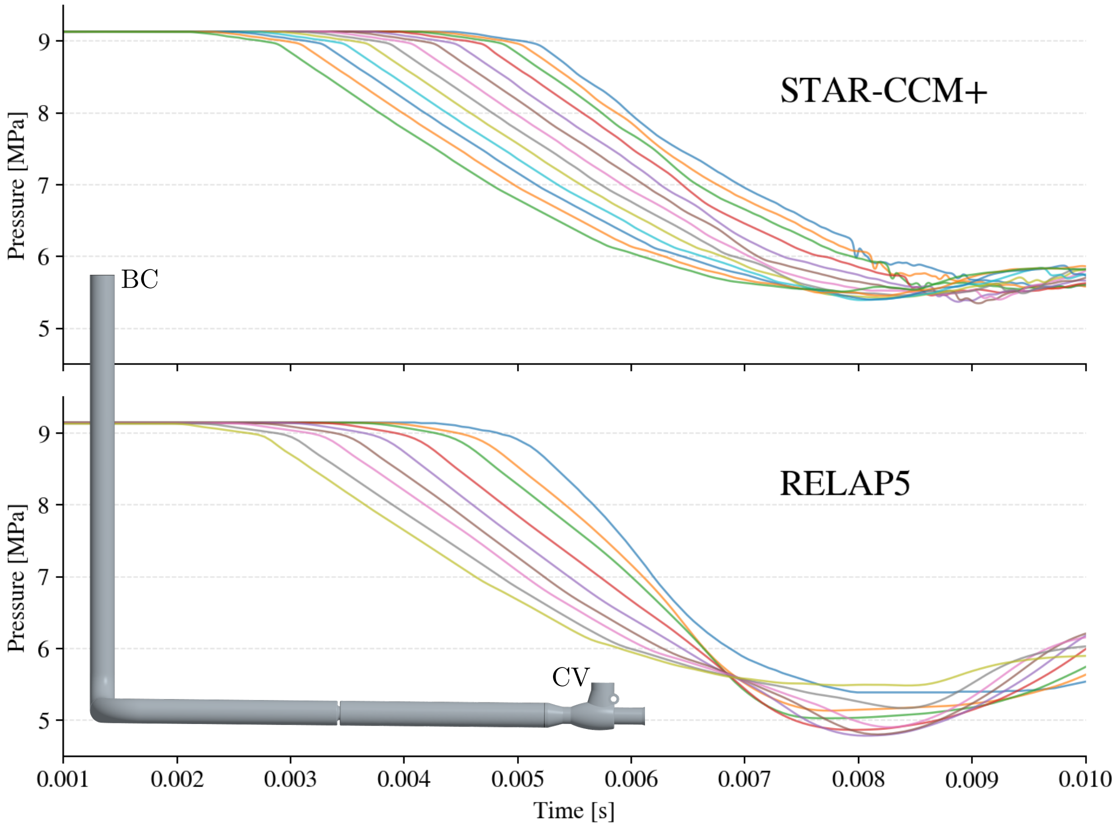


**Figure 4.15:** Pressure evolution at probe locations along the pipe between the pressure BC and the check valve (CV) during the initial phase. The insert shows the corresponding pipe segment.

The crossover of curves around $t = 0.007\,\mathrm{s}$ in the RELAP5 results indicates that the expansion wave has reflected off the rear surface of the closed check valve and propagated back towards the pressure BC, contributing to a further reduction in pressure. No such crossover is observed in STAR-CCM+, suggesting that this reflection does not occur in the 3D model.

The steeper pressure curves and wave reflections predicted by RELAP5 are likely related to the overestimated loss coefficient: the closed valve presents a larger obstacle to the flow, making it a more effective reflector. The complete absence of wave reflections in STAR-CCM+, however, is a surprising result that warrants further investigation.

## 4.5 Secondary Objective – Implementation of the `th_sr` Model

The following sections present the results of implementing the `th_sr` model. These results remain preliminary and would benefit from a broader set of simulations to properly constrain the regression model. They are nonetheless included here for completeness.

### 4.5.1 Loss Coefficients

As discussed in Sec. 4.4.4, the loss coefficient is highly relevant to the predicted flow field and check valve response. Fig. 4.16 shows the loss coefficient as a function of valve opening angle, for both forward and backward flow. The trend is the same for both flow directions: the loss coefficient increases rapidly as the valve approaches the fully closed position, while showing minimal variation for angles beyond the halfway open position. The power-law functions fitted to the data were determined by nonlinear least-squares regression using the `curve_fit` function from the SciPy library [18].

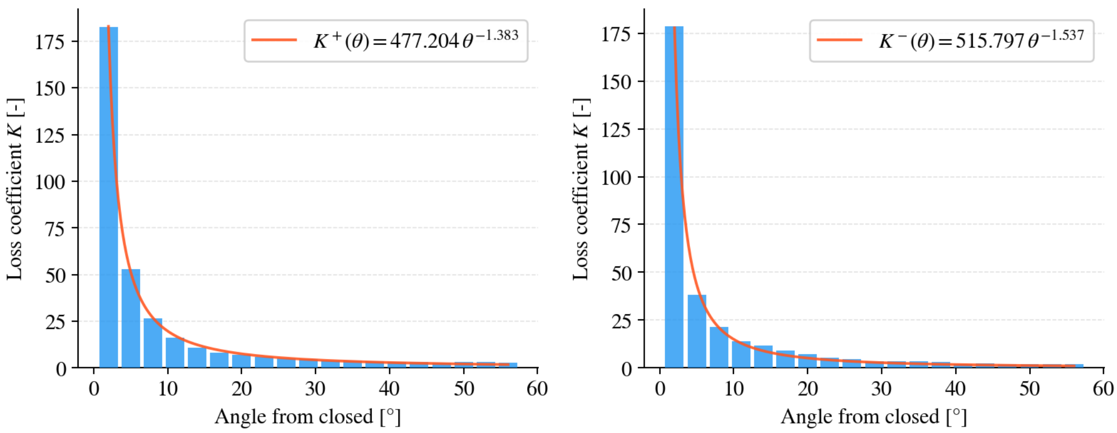


**Figure 4.16:** Loss coefficient $K$ as a function of valve angle for forward ($K^+$) and backward ($K^-$) flow directions as defined in Sec. 3.6.1, with fitted power-law functions.

The loss coefficient input to the force-based check valve model in RELAP5 is $K = 2.89$, obtained from CFD simulations for forward flow at the fully open valve position (56°).

### 4.5.2 Torque Coefficients

#### 4.5.2.1 Static

The static torque and the corresponding static torque coefficient for forward and backward flow velocities are shown in Fig. 4.17.

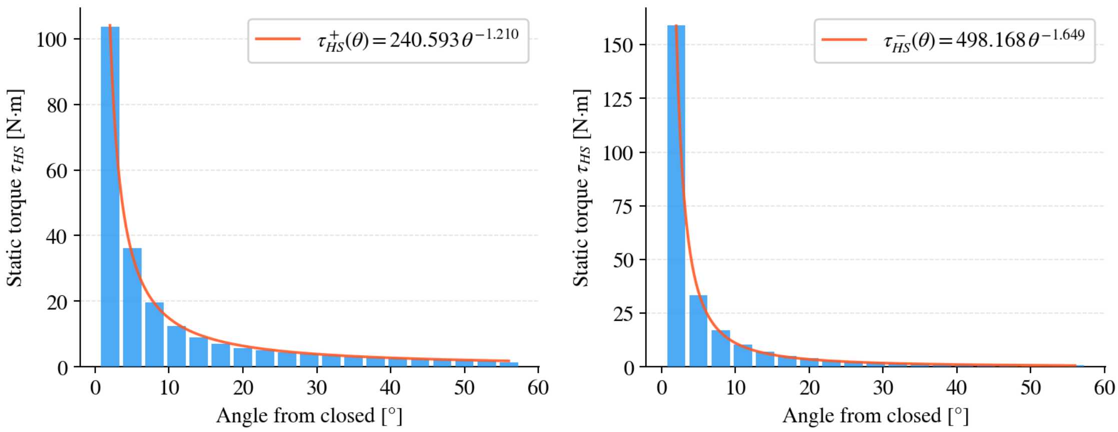


**(a)** Static torque $\tau_{HS}$

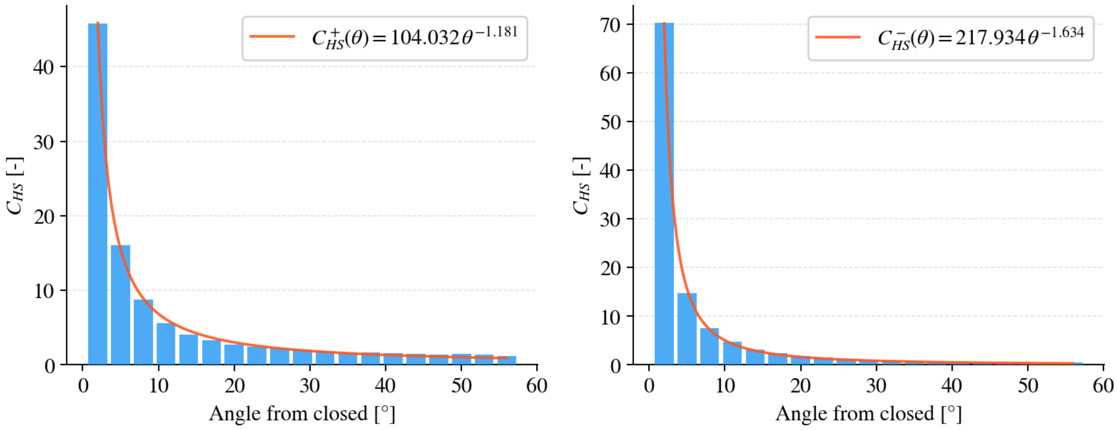


**(b)** Static torque coefficient $C_{HS}$

**Figure 4.17:** Static torque and corresponding static torque coefficient as a function of valve opening angle, with forward flow shown on the left and backward flow on the right of each panel.

The trend is similar to that of the loss coefficient, with a steep increase as the check valve nears its closed position and relatively flat as it approaches the fully open position. At $\theta = 2°$, the static torque is 53% larger for backward flow (159.01 Nm) than for forward flow (103.64 Nm).

#### 4.5.2.2 Rotational

The regression coefficients corresponding to each term in the regression model, Eq. (2.22),

$$\bar{C}_{HR} = k_1 + k_2\dot{\theta} + k_3 V + k_4\dot{\theta}V + k_5\dot{\theta}^2 + k_6 V^2$$

are shown as a function of valve angle in Fig. 4.18.

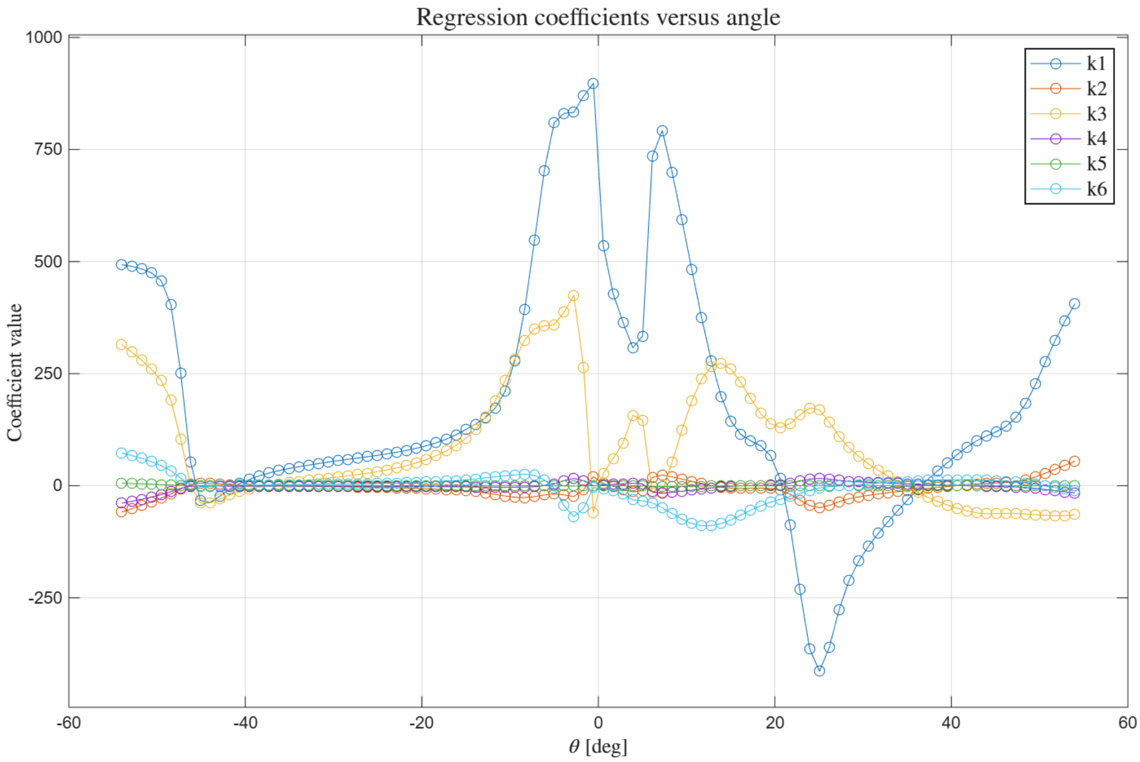


**Figure 4.18:** Regression coefficients $k_{1-6}$ as a function of angle.

Figure 4.19 shows the $R^2$ at each angle, indicating how well the extracted coefficients $k_{1-6}$ allow $\bar{C}_{HR}$ to approximate the actual value of $C_{HR}$, while Fig. 4.20 shows the distribution of regression data across the angle and velocity space from the nine cases in Table 3.1.

The $R^2$ values shown in Fig. 4.19 are consistently above 90% for angles in the range -36° to -12°, the range in which most of the data points in Fig. 4.20 are concentrated. Negative angles correspond to valve closure during reverse flow, which occurs in Cases 1–6 (Table 3.1): as the inlet velocity decelerates and eventually reverses, the valve — still closing — transitions from positive to negative $\theta$ (forward to reverse flow). Each of these cases therefore contributes data at positive angles only briefly, while deceleration is still in its early stage, before the flow reversal shifts the data into the negative-angle range. As a result, the positive-angle range 0 to 36° is populated almost entirely by Case 8, the only simulation in which the check valve opens from a fully closed position.

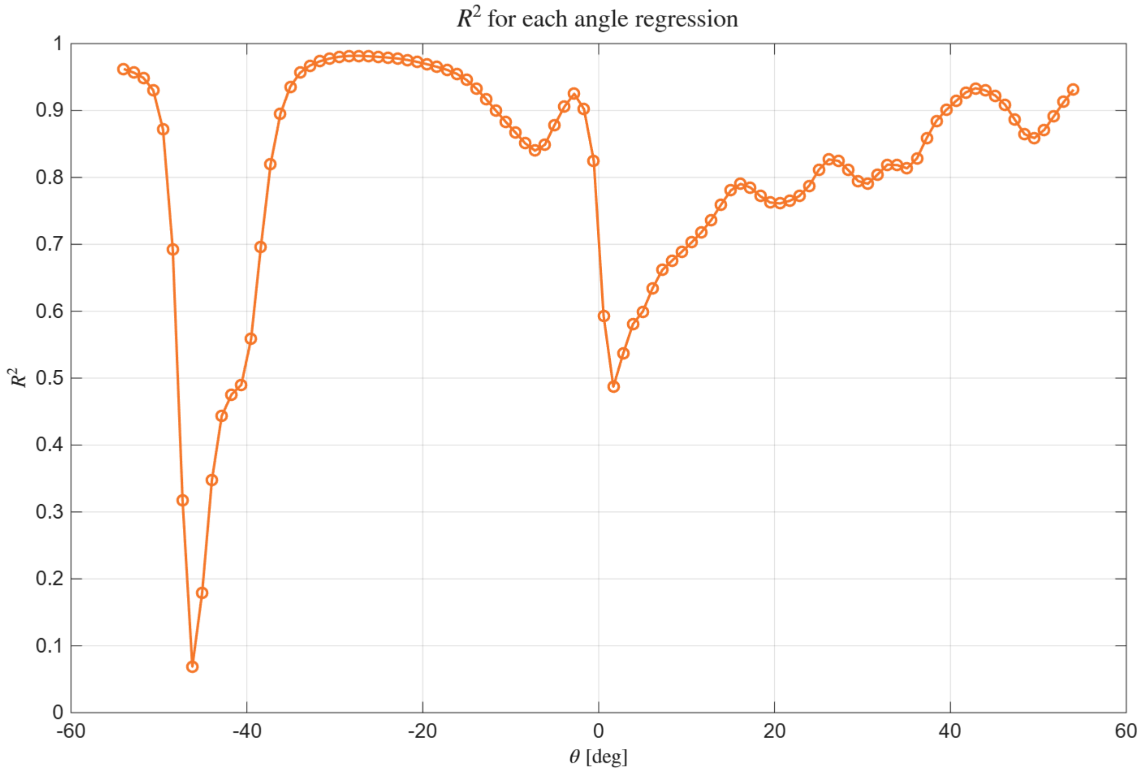


**Figure 4.19:** $R^2$ values quantifying how well the regression model approximates $C_{HR}$ at each angle.

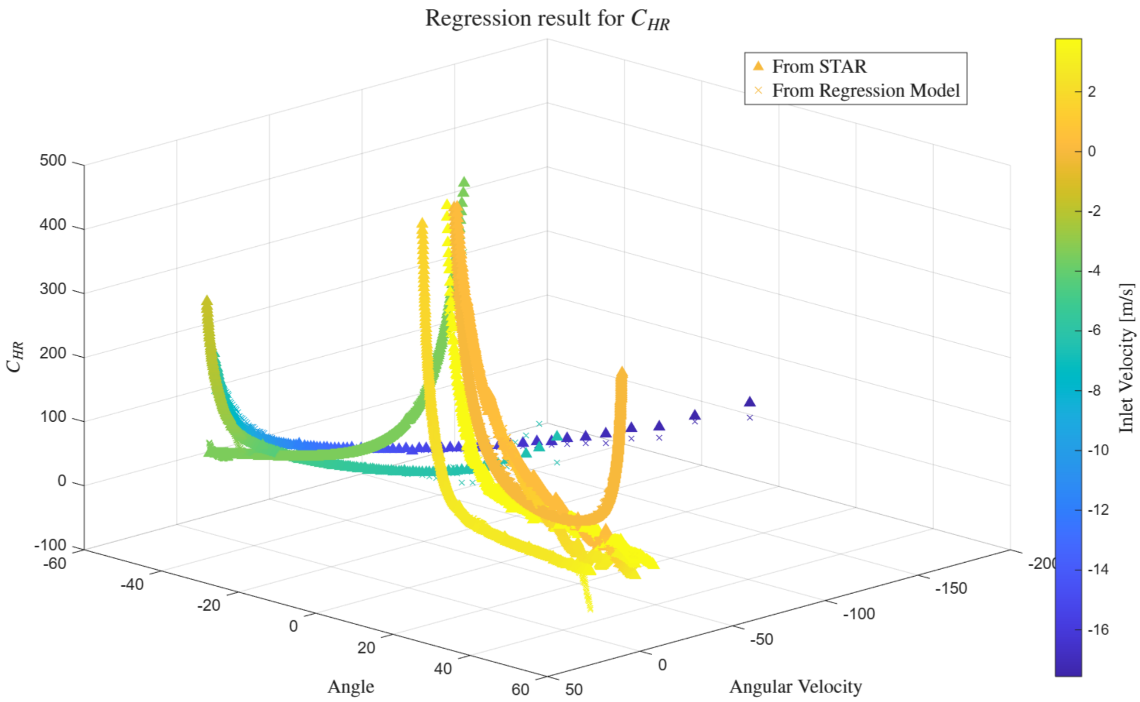


**Figure 4.20:** Regression data obtained from the cases in Table 3.1.

### 4.5.3 Valve Motion with the `th_sr` Check Valve Model

Overall, the `th_sr` model shows poor agreement with STAR-CCM+. However, the substantial difference between the two `th_sr` curves illustrates how sensitive the model is to the range of conditions used to fit the regression coefficients. Cases 1–6 do not include any simulations covering forward flow at intermediate opening angles, or valve opening from a fully closed position, leaving the regression model poorly constrained in this range and producing the unphysical, near-vertical transitions between nearly closed and nearly open positions visible in Fig. 4.21. When Cases 7–9 — which include the missing opening behavior — are added to the fit, the predicted valve motion changes substantially: the near-vertical transitions disappear and the check valve covers a considerably wider range of motion, though the trajectory still does not reflect physically realistic valve dynamics.

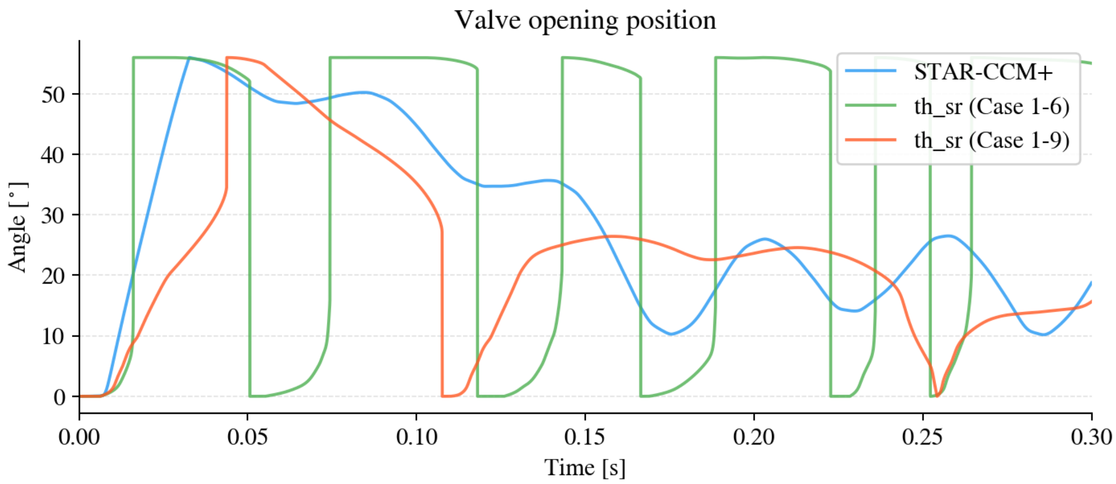


**Figure 4.21:** Comparison of valve trajectories between STAR-CCM+ and the RELAP5 `th_sr` model, using regression coefficients fitted with Cases 1–6 and Cases 1–9 (see Sec. 3.6.2 for case definitions).

## 4.6 Evaluation of RELAP5 Check Valve Models

### 4.6.1 Force-Based Model

The force-based RELAP5 model predicts significantly faster and more aggressive valve motion than STAR-CCM+: the check valve repeatedly cycles between open and closed in RELAP5, while in STAR-CCM+ it reaches a single full opening before settling into a damped oscillation around a partially open position within the simulated time. This discrepancy was traced to three main contributing factors, summarized below.

- **Underestimated effective inertia**: the absence of added mass and other hydrodynamic effects in the 1D model results in a lower effective resistance to angular acceleration, causing the valve to respond faster to flow variations than predicted by the 3D model (Sec. 4.4.2).
- **Overestimated force**: RELAP5 predicts a consistently larger hydraulic force acting on the check valve than STAR-CCM+ (Sec. 4.4.3), even when identical pressure BCs are applied in both models. This stems from the force formulation's use of fixed axial probe positions and a constant disc area normal to the flow, neither of which accounts for the valve's opening angle.
- **Loss coefficient deviates from STAR-CCM+ at intermediate angles**: the empirical correlation RELAP5 uses to scale $K$ away from the fully open position predicts a higher flow resistance than STAR-CCM+, causing the pressure differential to remain elevated for longer and driving more rapid valve opening (Sec. 4.4.4). Whether this reflects a limitation of the correlation itself or a mismatch between the correlation and the specific valve geometry studied here cannot be determined from the present results alone.

A consequence of the faster predicted motion is that the repeated valve closure events in RELAP5 generate sharp pressure peaks associated with the water hammer effect, whereas the check valve in STAR-CCM+ does not fully close within the simulated time. This suggests that the severity of the water hammer effect is exaggerated by the 1D model.

A related and unresolved finding concerns wave reflections within the pipe: RELAP5 predicts a clear reflection of the expansion wave off the closed check valve, plausibly linked to the deviating loss coefficient making the valve a more effective obstacle, whereas no such reflection is observed in STAR-CCM+ (Sec. 4.4.5). The complete absence of this reflection in the 3D model could not be explained from the present results and warrants further investigation.

The geometric correction to the hydraulic force (Sec. 4.4.3) demonstrates that targeted modifications to the RELAP5 model can improve agreement with STAR-CCM+. However, fully resolving the discrepancy would require addressing all three identified factors — inertia, force formulation, and loss coefficient scaling — through a more systematic calibration approach.

### 4.6.2 `th_sr` Model

The torque coefficients required to implement the `th_sr` model were successfully extracted from the 3D CFD simulations and tabulated as functions of valve angle (Sec. 4.5.2.1 and 4.5.2.2).

However, the resulting model does not reproduce physically realistic valve motion, primarily due to insufficient and unevenly distributed training data: the rotational torque regression is well constrained only for angles in the range -36° to -12°, while the positive-angle range is almost entirely represented by a single simulation (Case 8). This is reflected in the predicted valve trajectory, which shows unphysical, near-vertical transitions when fitted using only Cases 1–6; including Cases 7–9 removes these transitions and broadens the range of motion, but the trajectory still does not reflect physically realistic dynamics (Sec. 4.5.3). A broader and more systematically designed set of simulations would be required before the model could be meaningfully evaluated against STAR-CCM+.

# 5

# Conclusion

**The primary objective** of this thesis was to investigate the dynamic response of a swing check valve located far from an initiating pressure disturbance, comparing predictions from the RELAP5 1D model against compressible 3D CFD simulations in STAR-CCM+. The results show that RELAP5 predicts substantially faster and more aggressive valve motion than STAR-CCM+, with repeated cycling between open and closed, whereas STAR-CCM+ only reaches a single full opening before its motion settles into a damped oscillation around a partially open position within the simulated time.

This discrepancy was traced to three contributing factors: an underestimation of the valve's effective inertia in the 1D model, due to the absence of added mass and other hydrodynamic effects; an overestimated hydraulic force arising from RELAP5's force formulation, in which pressure extrapolated from fixed axial probe positions overestimates the pressure differential across the disc, while the assumption of constant projected disc area further inflates the resulting force — neither accounting for the valve's opening angle; and a deviation between the loss coefficient predicted by RELAP5's empirical angle-dependent scaling and the corresponding loss coefficient obtained from STAR-CCM+ at intermediate valve opening angles.

A consequence of the faster predicted motion is that RELAP5 generates repeated, sharp pressure spikes associated with the water hammer effect, while the corresponding STAR-CCM+ simulation does not predict the valve fully closing within the simulated time. The findings suggest that RELAP5 may overpredict the severity of the water hammer effect for this valve and location, although the degree of overprediction — and whether any clattering occurs at all under the conditions studied — remains uncertain given the differences identified between the two models.

Targeted modifications to the RELAP5 model, such as the geometric $\cos\theta$ scaling of the hydraulic force, demonstrate that the identified discrepancies can be reduced, but a systematic recalibration addressing inertia, force formulation, and loss coefficient scaling simultaneously would be required to achieve consistent agreement with the 3D simulations.

**The secondary objective** was to determine the torque coefficients required to implement the alternative `th_sr` check valve model in RELAP5, using steady-state and transient 3D CFD simulations. However, the resulting model does not reproduce physically realistic valve motion. This was traced to insufficient and unevenly distributed training data: the nine transient simulations performed provided coverage of the rotational torque coefficient only for valve closure during reverse flow, leaving the regression poorly constrained for valve opening and for forward flow at intermediate angles. The th_sr model could therefore not be meaningfully evaluated against STAR-CCM+ within the scope of this thesis.

## 5.1 Future Work

Based on the findings of this thesis, three directions for future work are suggested.

First, the force-based RELAP5 model could be modified to use a tabulated, angle-dependent loss coefficient rather than a single value based on the fully open position. The loss coefficients obtained as a function of valve angle in this thesis could serve as a starting point for such an implementation, and may help reduce the discrepancy identified between RELAP5 and STAR-CCM+ at intermediate opening angles.

Second, the complete absence of wave reflections in the STAR-CCM+ simulations, in contrast to the clear reflections predicted by RELAP5, remains unexplained and warrants further investigation, as it may point to additional, currently unidentified differences between the two models.

Third, implementing the th_sr model would benefit from a broader and more systematically designed set of transient simulations, specifically targeting forward flow at intermediate opening angles and valve opening from a fully closed position, to properly constrain the rotational torque regression coefficients across the full range of valve motion. The implementation approach closely mimicked that of Vavassori [15], but did not include sufficient coverage of the conditions specific to this problem; given more time, a more tailored implementation is recommended.

# Bibliography


[1] RELAP5/MOD3 Code Manual Volume II: User's Guide and Input Requirements. Technical Report NUREG/CR-5535, Volume II, U.S. Nuclear Regulatory Commission, Washington, DC, August 1995.

[2] Frank M. White. *Fluid Mechanics*. McGraw-Hill Education, New York, 8 edition, 2016.

[3] John D. Jr. Anderson. *Modern Compressible Flow: With Historical Perspective*. McGraw-Hill, New York, 3 edition, 2003.

[4] David C. Wilcox. *Turbulence Modeling for CFD*. DCW Industries, La Canada, California, 3 edition, 2006.

[5] Florian R. Menter. Two-equation eddy-viscosity turbulence models for engineering applications. *AIAA Journal*, 32(8):1598–1605, 1994.

[6] Henk Kaarle Versteeg and Weeratunge Malalasekera. *An Introduction to Computational Fluid Dynamics: The Finite Volume Method*. Pearson Education, Harlow, England, 2 edition, 2007.

[7] Jiri Blazek. *Computational Fluid Dynamics: Principles and Applications*. Butterworth-Heinemann, Oxford, 3 edition, 2015.

[8] Siemens Digital Industries Software. *STAR-CCM+ User Guide and Tutorials*. Siemens Digital Industries Software, 2020. Version 20.04.008-R8.

[9] M. Darwish, I. Sraj, and F. Moukalled. A coupled finite volume solver for the solution of incompressible flows on unstructured grids. *Journal of Computational Physics*, 228(1):180–201, 2009.

[10] Z.J. Chen and A.J. Przekwas. A coupled pressure-based computational method for incompressible/compressible flows. *Journal of Computational Physics*, 229(24):9150–9165, 2010.

[11] James L. Meriam, L. G. Kraige, and J. N. Bolton. *Engineering Mechanics: Dynamics*. Wiley, Hoboken, NJ, 9 edition, 2020.

[12] John N. Newman. *Marine Hydrodynamics*. The MIT Press, Cambridge, Massachusetts, 40th anniversary edition edition, 2018.

[13] Anna Jarenfors. Pamrel manual. Internal Report FSDFI3020133-01, FS Dynamics, Sweden, 2025. Approved by Magnus Ohlson, Revision 01 J.

[14] Guohua Li and Jim Liou. Swing check valve characterization and modeling during transients. *Journal of Fluids Engineering-transactions of The Asme - J FLUID ENG*, 125, 11 2003.

[15] Giacomo Vavassori. Swing check valve characterization: 3D CFD validation of one dimensional models used in RELAP5. Master's thesis, KTH Royal Institute of Technology, Stockholm, Sweden, 2017.

[16] RELAP5 Development Team. RELAP5/MOD3 Code Manual, Volume IV: Models and Correlations. Technical Report NUREG/CR-5535 Vol. 4, INEL-95/0174 Vol. 4, Idaho National Engineering Laboratory, Idaho Falls, Idaho, USA, August 1995.

[17] National Institute of Standards and Technology. NIST Chemistry WebBook, SRD 69. `https://webbook.nist.gov`, 2023. Accessed: 2026.

[18] Pauli Virtanen et al. SciPy 1.0: Fundamental algorithms for scientific computing in Python. *Nature Methods*, 17:261–272, 2020.

[19] Felix Wiebe. Torque limited simple pendulum: Underactuated system. `https://github.com/dfki-ric-underactuated-lab/torque_limited_simple_pendulum`, 2022. BSD-3-Clause license. Accessed: 2026.

# A

# Analytical solution for drop test

The following is the Python code made for the analytical solution used for the drop test in Sec. 4.2. It is based on the torque-limited simple pendulum framework [19], and has been modified to model the dynamics of a swing check valve under the influence of gravity and buoyancy.

```python
import numpy as np
import matplotlib.pyplot as plt

class PendulumPlant:
    def __init__(self, mass=1.0, length=0.5, damping=0.1, gravity=9.81,
                 coulomb_fric=0.0, inertia=None, torque_limit=np.inf):
        self.m = mass
        self.l = length
        self.b = damping
        self.g = gravity
        self.coulomb_fric = coulomb_fric
        if inertia is None:
            self.inertia = mass * length * length
        else:
            self.inertia = inertia
        self.torque_limit = torque_limit
        self.dof = 1
        self.n_actuators = 1
        self.base = [0, 0]
        self.n_links = 1
        self.workspace_range = [[-1.2*self.l, 1.2*self.l],
                                [-1.2*self.l, 1.2*self.l]]

    def forward_dynamics(self, state, tau):
        torque = np.clip(tau, -np.asarray(self.torque_limit),
                         np.asarray(self.torque_limit))
        accn = (torque - self.m * self.g * self.l * np.sin(state[0]) -
                self.b * state[1] -
                np.sign(state[1]) * self.coulomb_fric) / self.inertia
        return accn

pendulum = PendulumPlant(mass=1.5167,
                         length=0.0567842,    # pivot-to-CoM distance [m]
                         damping=0.0,         # no damping
                         gravity=9.81,
                         coulomb_fric=0.0,    # no friction
                         inertia=0.0067,
```

```
                         torque_limit=np.inf)

theta = np.deg2rad(90.0)   # fully open: CoM horizontal from pivot
omega = 0.0
theta_closed = np.deg2rad(34.0)  # fully closed: 90 - 56 = 34 deg

dt = 1e-6
t_end = 0.2
n_steps = int(t_end / dt)

t_hist, theta_hist, omega_hist = [], [], []
seat_hit_time = None

# -------------------------
# Fluid / buoyancy parameters
# -------------------------
rho_water = 991.0        # kg/m^3, water at 50 deg C
rho_valve = 7900.0       # kg/m^3, steel
V_valve = pendulum.m / rho_valve
F_b = rho_water * pendulum.g * V_valve

# -------------------------
# Simulation loop
# -------------------------
for i in range(n_steps):
    t = i * dt
    state = [theta, omega]

    tau_buoyancy = (rho_water / rho_valve) * pendulum.m * pendulum.g \
                   * pendulum.l * np.sin(theta)

    alpha  = pendulum.forward_dynamics(state, tau=tau_buoyancy)
    omega += alpha * dt
    theta += omega * dt

    # Mechanical stop at fully closed position
    if theta <= theta_closed:
        theta = theta_closed
        if omega < 0.0:
            if seat_hit_time is None:
                seat_hit_time = t
            omega = 0.0

    t_hist.append(t)
    theta_hist.append(np.rad2deg(theta) - 34.0)
    omega_hist.append(omega)
```

# B

# Coupled vs. Segregated Solver during Transient Simulations

This appendix shows the comparison between the coupled and segregated flow solvers referenced in Sec. 3.5.1. Both solvers were evaluated using the $k$-$\omega$ SST turbulence model under identical BCs, with the resulting pressure histories compared against RELAP5 at Probe 1 and Probe 2, whose locations are shown in Fig. 4.4b.

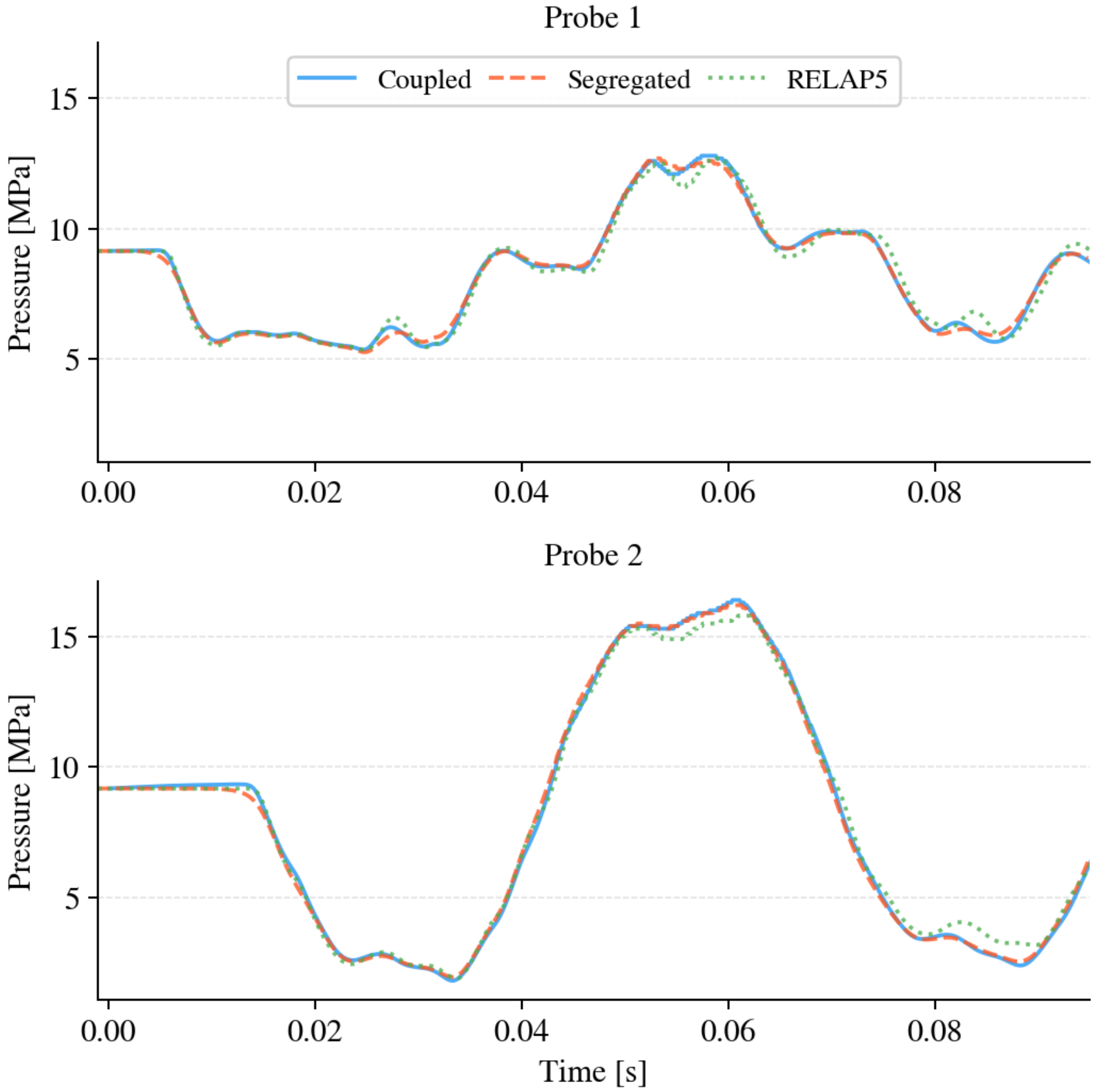


**Figure B.1:** Comparison of pressure between the coupled and segregated solvers, compared against the RELAP5 prediction at Probe 1 and Probe 2.

# C

# MATLAB Script for Regression Coefficient Calculation

The following MATLAB script was used to compute the regression coefficients $k_{1-6}(\theta_i)$ from the transient simulation data, as described in Sec. 3.6.2. Prior to the regression, outliers and invalid data points are removed based on predefined thresholds. For each discrete valve angle $\theta_i$, a weighted least-squares regression is then performed on the data points within a Gaussian-weighted neighborhood of $\theta_i$, yielding the coefficients of the model in Eq. 2.22. The script also evaluates the goodness of fit ($R^2$) at each angle and generates plots comparing the regression model against the CFD data.

```
filename = 'dataset.xlsx';

theta_min = -54;
theta_max = 54;
n_angles  = 98;

output_file = 'k_coefficients_table.txt';

theta_bandwidth = 2;

theta_header   = 'relap_angle';
omega_header   = 'ang_vel';
V_header       = 'inlet_vel';
CHR_header     = 'C_HR';
case_header    = 'CASE_NR';

dataset = readtable(filename, ...
    'VariableNamingRule', 'preserve', ...
    'ReadVariableNames', true, ...
    'Range', 'A1:Y100000');

theta   = dataset.(theta_header);
omega   = dataset.(omega_header);
V       = dataset.(V_header);
CHR     = dataset.(CHR_header);
case_nr = dataset.(case_header);

valid = isfinite(theta) & isfinite(omega) & ...
        isfinite(V) & isfinite(CHR) & isfinite(case_nr) ...
        & CHR <= 500 ...
```

```
        & abs(theta) >= 3 ...
        & abs(theta) <= 54 ...
        & ~ismember(case_nr, []);

removed_cases = unique(case_nr(~valid));
removed_cases = removed_cases(isfinite(removed_cases));
remaining_cases = unique(case_nr(valid));
remaining_cases = remaining_cases(isfinite(remaining_cases));
fully_eliminated = removed_cases(~ismember(removed_cases, remaining_cases));

fprintf('Cases used: %s\n', num2str(remaining_cases(:)'))
if ~isempty(fully_eliminated)
    fprintf('Eliminated cases: %s\n', num2str(fully_eliminated(:)'))
else
    fprintf('No cases eliminated.\n')
end

theta = theta(valid);
omega = omega(valid);
V     = V(valid);
CHR   = CHR(valid);

angle_range = theta >= theta_min & theta <= theta_max;

theta = theta(angle_range);
omega = omega(angle_range);
V     = V(angle_range);
CHR   = CHR(angle_range);

theta_bins = linspace(theta_min, theta_max, n_angles)';

coeff_table = zeros(length(theta_bins), 7);
R2_table    = zeros(length(theta_bins), 3);

X = [ ...
    ones(size(omega)), ...
    omega, ...
    V, ...
    omega .* V, ...
    omega.^2, ...
    V.^2 ...
];

for i = 1:length(theta_bins)
    theta_i = theta_bins(i);
    w = exp(-0.5*((theta - theta_i)/theta_bandwidth).^2);
    Wsqrt = sqrt(w);
    Xw   = X   .* Wsqrt;
    CHRw = CHR .* Wsqrt;
    k = Xw \ CHRw;
    CHR_pred = X * k;
    CHR_mean_w = sum(w .* CHR) / sum(w);
    SS_res = sum(w .* (CHR - CHR_pred).^2);
    SS_tot = sum(w .* (CHR - CHR_mean_w).^2);
    R2 = 1 - SS_res / SS_tot;
    coeff_table(i,:) = [theta_i, k'];
    R2_table(i,:)    = [theta_i, R2, sum(w > 0.01)];
```

```
end

disp('Coefficient table:')
disp('theta        k1         k2         k3         k4         k5         k6')
disp(coeff_table)

header = 'theta k1 k2 k3 k4 k5 k6';

fid = fopen(output_file, 'w');
fprintf(fid, '%s\n', header);
fclose(fid);

dlmwrite(output_file, coeff_table, '-append', ...
         'delimiter', '\t', 'precision', 10);

figure()
plot(R2_table(:,1), R2_table(:,2), 'b-o', ...
     'LineWidth', 1.5, 'MarkerSize', 6)
xlabel('\theta [deg]')
ylabel('R^2')
title('R^2 for each angle regression')
grid on

average_R2 = mean(R2_table(:,2), 'omitnan');
fprintf('Average R2 = %.4f\n', average_R2)

figure()
plot(coeff_table(:,1), coeff_table(:,2), '-o', ...
     coeff_table(:,1), coeff_table(:,3), '-o', ...
     coeff_table(:,1), coeff_table(:,4), '-o', ...
     coeff_table(:,1), coeff_table(:,5), '-o', ...
     coeff_table(:,1), coeff_table(:,6), '-o', ...
     coeff_table(:,1), coeff_table(:,7), '-o')
xlabel('\theta [deg]')
ylabel('Coefficient value')
title('Regression coefficients versus angle')
legend('k1','k2','k3','k4','k5','k6', 'Location', 'best')
grid on

CHR_reg = zeros(size(CHR));

for j = 1:length(CHR)
    [~, idx] = min(abs(coeff_table(:,1) - theta(j)));
    k = coeff_table(idx, 2:7);
    CHR_reg(j) = k(1) ...
        + k(2)*omega(j) ...
        + k(3)*V(j) ...
        + k(4)*omega(j)*V(j) ...
        + k(5)*omega(j)^2 ...
        + k(6)*V(j)^2;
end

figure()
hold on
scatter3(omega, theta, CHR, 45, V, '^', 'filled')
scatter3(omega, theta, CHR_reg, 25, V, 'x')
xlabel('Angular Velocity')
```

```
ylabel('Angle')
zlabel('C_{HR}')
title('Regression result for C_{HR}')

legend('From STAR', 'From Regression Model', 'Location', 'best')

cb = colorbar;
cb.Label.String = 'Inlet Velocity [m/s]';

grid on
view(135, 25)
hold off
```

# D

# Time-Step Sensitivity Study

Fig. D.1 shows the effect of the time-step size on the valve opening time and the mass flow oscillations in the Pressure Wave with Active Valve section (Sec. 4.3). A smaller time step results in earlier valve opening, consistent with faster pressure wave propagation, while the larger adaptive time step introduces a visible delay in the mass flow oscillations relative to RELAP5.

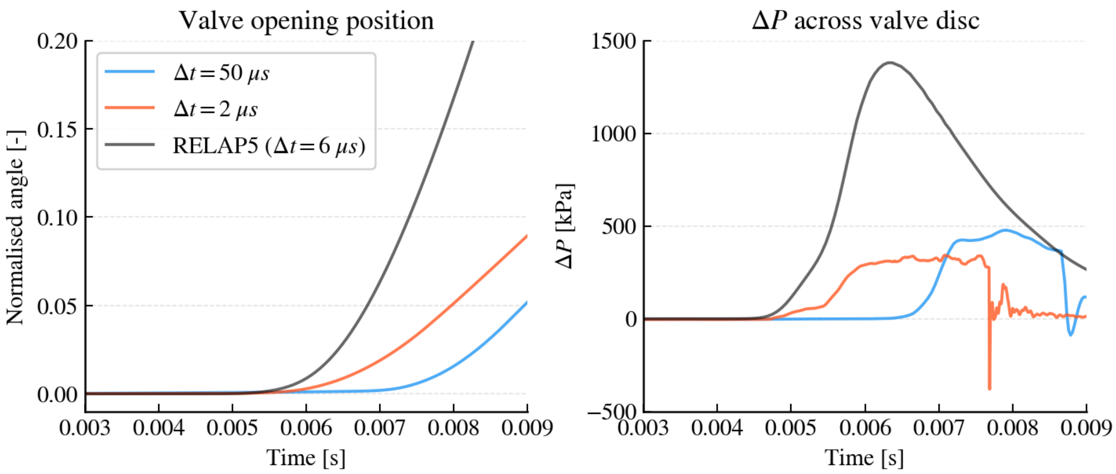


**(a)** Valve opening time for different time-step sizes compared to RELAP5.

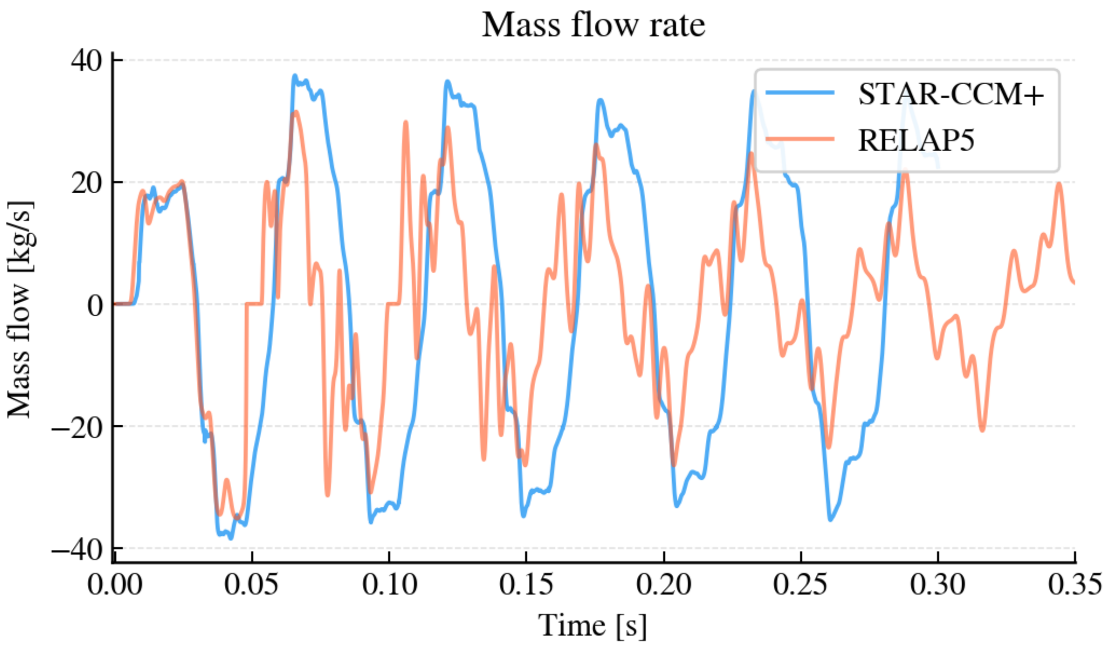


**(b)** Delay in mass flow oscillations when using the adaptive time step ($\Delta t = [1, 5] \times 10^{-5}$ s) compared to RELAP5

.

**Figure D.1:** Effect of time-step size on the active valve simulation results.

# E

# Motion of Check Valve with Reduced Density

This appendix supplements the discussion in Sec. 4.4.2, showing the valve trajectory from a STAR-CCM+ simulation in which the check valve density, and consequently the moment of inertia tensor, were reduced by %. The purpose of this simulation was to assess the sensitivity of the valve dynamics to the moment of inertia. As shown in Fig. E.1, the trajectory during the initial opening phase shows no significant difference compared to the original case, suggesting that the moment of inertia of the check valve in STAR-CCM+ is already small enough that further reductions have little influence on the dynamics.

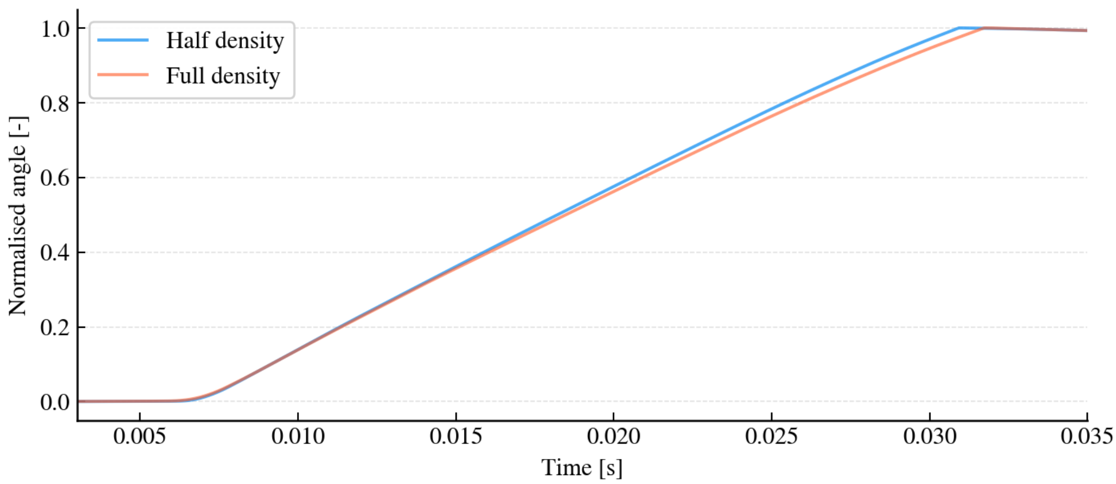


**Figure E.1:** Valve trajectory during the initial opening phase with the check valve density reduced by 50%, compared against the nominal STAR-CCM+ case.

# F

# Pressure Probe Positions

The axial positions of the pressure probes used to reproduce the RELAP5 force formulation in STAR-CCM+, as discussed in Sec. 4.4.3, are shown in Fig. F.1. The probes were placed at axial locations similar to the upstream and downstream measurement positions defined in the RELAP5 force formulation (Sec. 2.3.1).

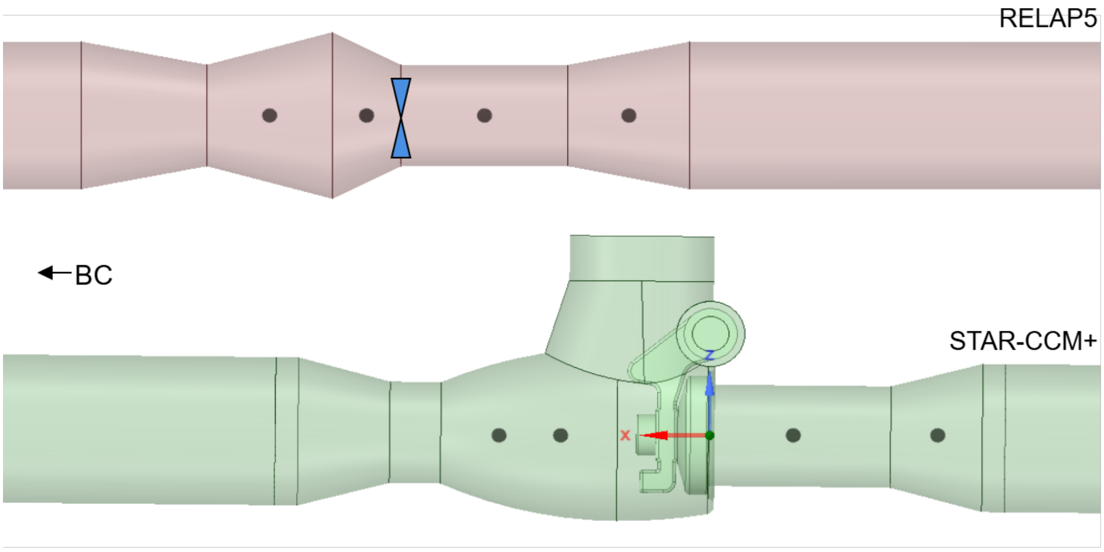


**Figure F.1:** Axial positions of the pressure probes used to reproduce the RELAP5 force formulation in STAR-CCM+, shown relative to the check valve disc.

# G

# Pressure Equalization During Active Valve Simulation

This appendix supplements the discussion in Sec. 4.4.4.

The sudden increase in mass flow at $t \approx 0.0086\,\mathrm{s}$ coincides with the pressure drop visible in Fig. 4.13, and occurs when the check valve fully separates from its seat and the gap closure model reactivates the previously deactivated cells. The pressure equalization process is illustrated in Fig. G.1.

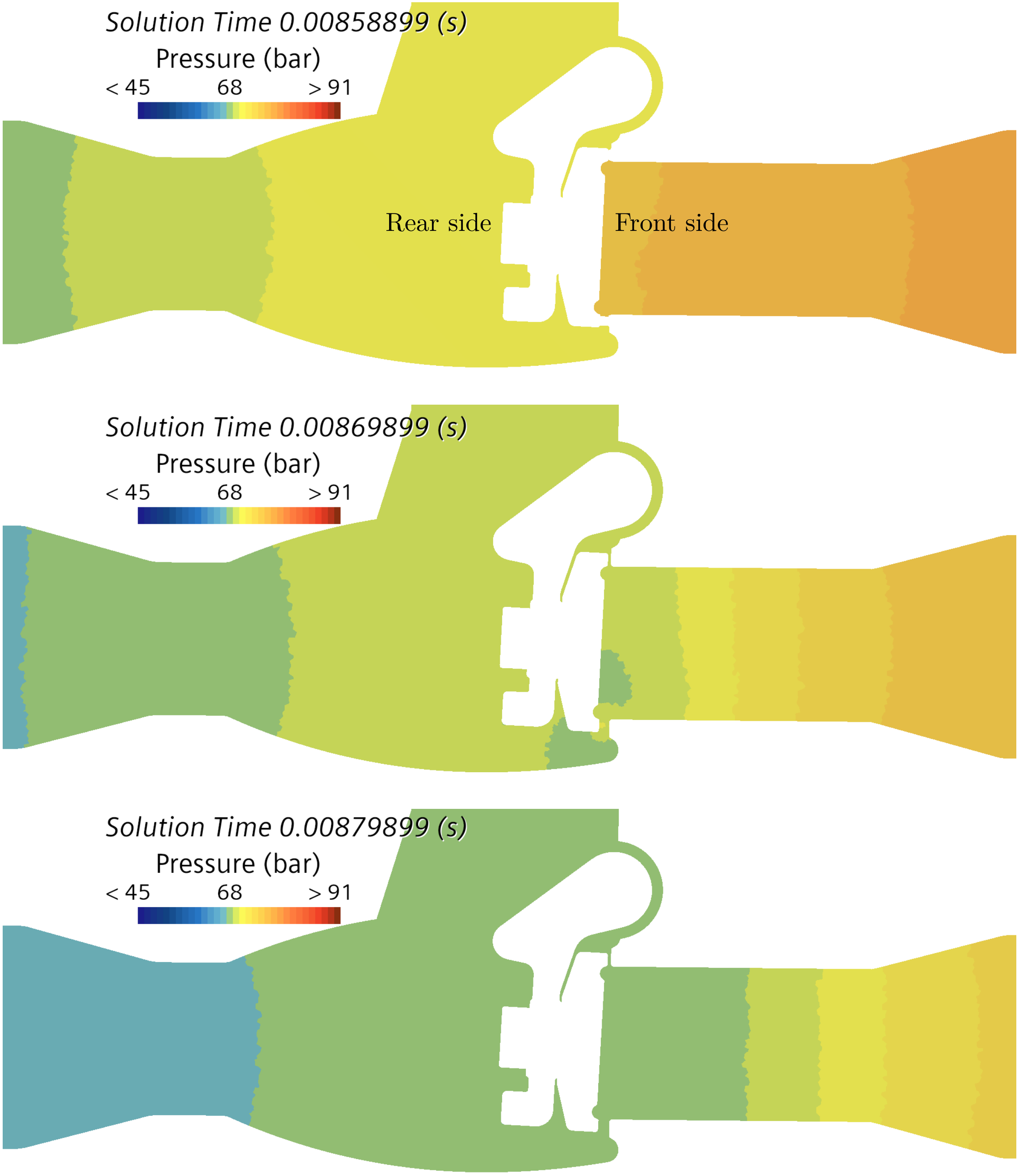


**Figure G.1:** Pressure equalization as the gap opens. The time step between each frame is 0.1 ms.

DEPARTMENT OF MECHANICS AND MARITIME SCIENCES
CHALMERS UNIVERSITY OF TECHNOLOGY
Gothenburg, Sweden
www.chalmers.se

CHALMERS
UNIVERSITY OF TECHNOLOGY